Earth and Planetary Science Letters 496 (2018) 142–158

Contents lists available at ScienceDirect

Earth and Planetary Science Letters

www.elsevier.com/locate/epsl

A Neogene history of mantle convective support beneath Borneo

Gareth G. Roberts [a,*], Nicky White [b,*], Mark J. Hoggard [b], Patrick W. Ball [b], Conor Meenan [b]

[a] Department of Earth Science and Engineering, Imperial College London, London, UK
[b] Bullard Laboratories, Department of Earth Sciences, University of Cambridge, Cambridge, UK

A R T I C L E I N F O

Article history:
Received 6 December 2017
Received in revised form 18 May 2018
Accepted 24 May 2018
Available online 6 June 2018
Editor: F. Moynier

Keywords:
Borneo
uplift
river profiles
Neogene
mantle convection
inverse modeling

A B S T R A C T

Most, but not all, geodynamic models predict 1–2 km of mantle convective draw-down of the Earth's surface in a region centered on Borneo within southeast Asia. Nevertheless, there is geomorphic, geologic and geophysical evidence which suggests that convective uplift might have played some role in sculpting Bornean physiography. For example, a long wavelength free-air gravity anomaly of +60 mGal centered on Borneo coincides with the distribution of Neogene basaltic magmatism and with the locus of sub-plate slow shear wave velocity anomalies. Global positioning system measurements, an estimate of elastic thickness, and crustal isostatic considerations suggest that regional shortening does not entirely account for kilometer-scale regional elevation. Here, we explore the possible evolution of the Bornean landscape by extracting and modeling an inventory of 90 longitudinal river profiles. Misfit between observed and calculated river profiles is minimized by smoothly varying uplift rate as a function of space and time. Erosional parameters are chosen by assuming that regional uplift post-dates Eocene deposition of marine carbonate rocks. The robustness of this calibration is tested against independent geologic observations such as thermochronometric measurements, offshore sedimentary flux calculations, and the history of volcanism. A calculated cumulative uplift history suggests that kilometer-scale Bornean topography grew rapidly during Neogene times. This suggestion is corroborated by an offshore Miocene transition from carbonate to clastic deposition. Co-location of regional uplift and slow shear wave velocity anomalies immediately beneath the lithospheric plate implies that regional uplift could have been at least partly generated and maintained by temperature anomalies within an asthenospheric channel.

1. Introduction

It is generally agreed that convective circulation of the Earth's mantle generates and maintains some component of surface topography (e.g. Pekeris, 1935; Richards and Hager, 1984; McKenzie, 2010; Müller et al., 2018). This component is often referred to as dynamic topography and it is expected to vary as a function of space and time. A significant corollary is that the history of vertical motions of the Earth's surface are indirectly recorded by the stratigraphic record. Despite more than 30 yr of geodynamic modeling, there is considerable debate about the amplitude and wavelength of present-day dynamic topography (see e.g. Steinberger, 2007; Spasojevic and Gurnis, 2012; Yang and Gurnis, 2016; Steinberger et al., 2017; Müller et al., 2018). A significant example of this lack of consensus concerns the history of regional epeirogeny across southeast Asia.

The present-day plate tectonic setting of this region is undoubtedly complex (see, e.g., Hall and Nichols, 2002; Replumaz et al., 2004; Hall, 2009; Cullen, 2010; Hall and van Hattum, 2010). Numerous fragments of subducted oceanic lithosphere, volcanic arcs, back-arc sedimentary basins, and flexural foreland basins form a kalaeidoscopic framework that has undoubtedly had a rapidly evolving history during Mesozoic and Cenozoic times. Global dynamic topographic models consistently predict that vertical motions of this region are dominated by a long wavelength (i.e. 10^3–10^4 km) convectively maintained depression or draw-down that is up to 2 km deep (Fig. 1; Lithgow-Bertolloni and Gurnis, 1997; Steinberger, 2007; Spasojevic and Gurnis, 2012; Flament et al., 2013; Yang and Gurnis, 2016). This draw-down is thought to be maintained by the presence of many cold slabs of subducted oceanic lithosphere (e.g. Yang et al., 2016). According to Stokes' law, the resultant mass excess generates and maintains large-scale downwelling within the viscously deformable mantle, which produces and maintains surface draw-down (compare Fig. 1c and d). It is important to emphasize that this topic is a rapidly evolving one and that several alternative dynamic topographic models predict

* Corresponding authors.
E-mail addresses: gareth.roberts@imperial.ac.uk (G.G. Roberts), njw10@cam.ac.uk (N. White).

https://doi.org/10.1016/j.epsl.2018.05.043
0012-821X/© 2018 Published by Elsevier B.V.

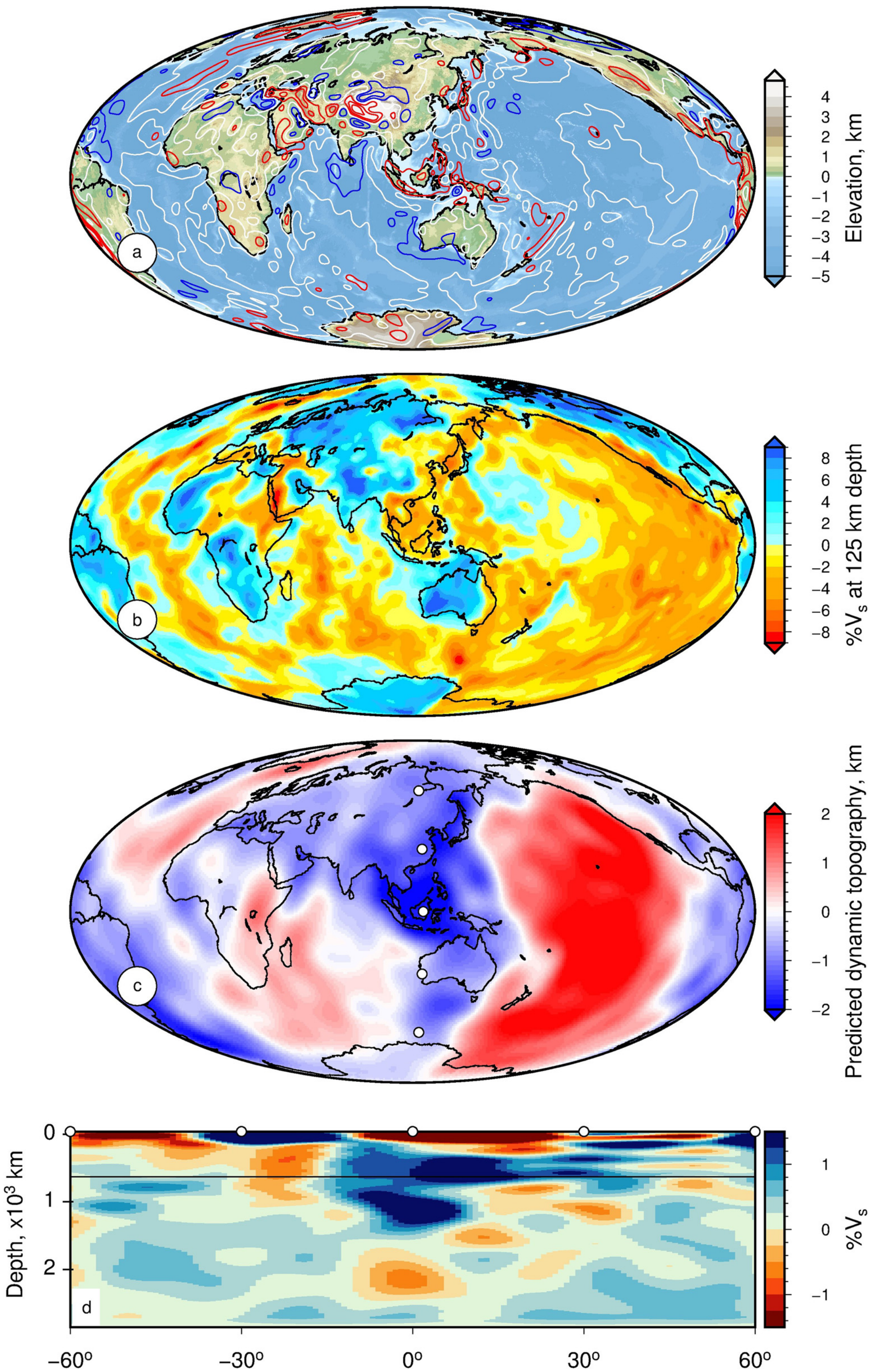

Fig. 1. (a) Global topographic map superimposed with long wavelength (730–9000 km) free-air gravity field from ETOPO5 and GGMO3C databases, respectively (Tapley et al., 2005; Hoggard et al., 2016). Red/white/blue contours = positive/zero/negative gravity anomalies at 30 mGal intervals. (b) Horizontal slice through SL2013sv shear velocity tomographic model where percentage anomaly is with respect to AK135 model (Schaeffer and Lebedev, 2013). (c) Predicted dynamic topography calculated by Steinberger (2007), which is broadly representative of other models (e.g. Müller et al., 2018). Open circles = positions along transect shown in panel (d). (d) Vertical slice along transect highlighted in panel (c) which shows shear wave velocity anomalies from S20RTS model of Ritsema et al. (1999) that was used to calculate panel (c). Black line = 670 km mantle discontinuity. (For interpretation of the colors in the figure(s), the reader is referred to the web version of this article.)

that a region encompassing Borneo underwent significant Neogene uplift (see, e.g., Yang et al., 2016; Steinberger et al., 2017; Müller et al., 2018).

One way of testing the veracity of different predictive dynamic topographic models is to measure residual depth anomalies of oceanic lithospheric fragments throughout this region. Wheeler and White (2002) used a compilation of shiptrack measurements to determine the distribution of residual depths throughout a region that stretches from the Sea of Japan to the Banda Sea, and from Thailand to the Mariana Islands. They suggested that water-loaded residual depth anomalies were ± 300 m and that these anomalies varied on wavelengths which are generally shorter than those predicted by mantle flow models. Subsequently, Hoggard et al. (2016) extended this analysis northeastward into the Pacific Ocean and southwestward into the Indian Ocean. They confirmed that while there is evidence for negative dynamic topographic anomalies, amplitudes rarely exceed 300 m at low spherical harmonic degrees (i.e. 1–3).

The island of Borneo occupies a key position at the center of this predicted draw-down (Fig. 1; Steinberger, 2007; Spasojevic and Gurnis, 2012). Here, we examine a combination of geomorphic, geologic and geophysical observations in order to estimate the history of vertical movements and to suggest how these vertical movements are generated and maintained. The centerpiece of our analysis is inverse modeling of a drainage inventory with a view to determining the distribution of cumulative uplift as a function of space and time subject to independent observational constraints. Finally, by converting observed shear velocity anomalies into temperature and by carrying out simple isostatic calculations, we explore plausible mechanisms of regional uplift (e.g. horizontal shortening of crust and lithosphere, magmatic underplating, anomalously hot asthenospheric mantle).

2. Regional framework

Bornean physiography is characterized by a central spine of regional uplift flanked by wide and flat coastal plains, especially around the southwestern coastline (Fig. 2a). Regional heatflow is anomalously high and a long wavelength free-air gravity anomaly of +60 mGal is centered on Borneo itself (Fig. 1a). Surrounding fragments of oceanic lithosphere are characterized by short wavelength negative residual depth anomalies that can be locally substantial (e.g. −600 m within the South China Sea to the north of Borneo; −800 m and −1.5 km within the Sulu and Celebes seas to the east of Borneo, respectively; and −300 m to +300 m within the Java Sea to the south of Borneo).

Earthquake tomographic models show that slow shear wave velocity anomalies lie beneath a region encompassing Borneo (Figs. 1b and 2c). Slow velocities are recorded between the northern edge of the South China Sea and the Banda arc down to a depth of about 200 km (Fig. 2c; Replumaz et al., 2004). Further south, a widespread fast velocity anomaly is probably associated with northward subduction of the Indian plate. The presence of slow shear wave velocities within the upper mantle beneath Borneo suggest that sub-plate buoyancy anomalies could play a role in generating some proportion of its topography (e.g. Fig. 2c; Schaeffer and Lebedev, 2013).

These general observations raise two significant issues. First, how does the thickness and rigidity of the Bornean crust and lithosphere affect the way in which sub-plate density anomalies are manifest at the Earth's surface? Secondly, if regional topography is generated and maintained by sub-plate buoyancy, when and how did this buoyancy develop?

2.1. Admittance analysis

The relationship between topography and gravity can be used to assess the way in which crustal and lithospheric loads are supported. The existence of a positive long wavelength ($\sim 10^3$ km) free-air gravity anomaly suggests that sub-lithospheric mantle may play a role in supporting Borneo's long wavelength topography (Fig. 1a). To estimate potential dynamic support and elastic thickness, T_e, we first calculate the admittance, Z, as a function of k, the wavenumber (Fig. 3). $Z(k)$ is calculated by spectrally analyzing the SRTM_30_plus topographic model and the Eigen-6C_3stat gravity model (Fig. 3a–b; Becker et al., 2009; McKenzie, 2010; Forste et al., 2012). The observed values of $Z(k)$ and the degree of coherence between the topographic and gravity fields are shown in Fig. 3c and e, respectively. At short wavelengths, the coherence between both fields is high and Z tends toward a constant value of ~ 100 mGal km^{-1}. This value is thought to depend upon the uncompensated density of the upper crust (i.e. $Z \rightarrow 2\pi\rho_{cu}g$ where ρ_{cu} is the density of the upper crust). At wavelengths of ~ 100 km, Z starts to decrease. The start and shape of this 'roll-over' determines the value of T_e. At the longest wavelengths, Z increases again toward a value of 50–75 mGal km^{-1}.

Although the coherence between the two fields decreases at wavelengths centered on 200 km, it is sufficiently high to justify flexural modeling of $Z(k)$. Sparse receiver function analyses on the coastal plain suggest that crustal thickness is 20–35 km (Fig. 2b). Here, we assume that the crust and the upper crust are 30 and 15 km thick, respectively (Lipke, 2008). These values are broadly consistent with a regional shear wave velocity model and with the results of a seismic wide-angle experiment located offshore northwest Borneo (Franke et al., 2008; Tang and Zheng, 2013). Density of the upper crust, $\rho_{cu} = 2.45$ Mg m^{-3}, is determined by the value of Z at the shortest wavelengths and we assume that the density of the lower crust is 2.9 Mg m^{-3}. An elastic model with $T_e = 7 \pm 3$ km yields an acceptable fit to observed values of Z at wavelengths of < 300 km (Fig. 3c). The value of T_e does trade off positively with the percentage of internal loading but a shallow global minimum exists for internal loading of 31%. At wavelengths approaching 10^3 km, Z tends toward 50–75 mGal km^{-1}, a value which is not accounted for by the elastic model. This positive departure from behavior predicted by the elastic model is often observed (McKenzie, 2010). It implies that at these long wavelengths, > 1 km of Bornean topography could be supported by sub-crustal (i.e. mantle) density variations.

2.2. Neogene stratigraphy and magmatism

It has been previously been suggested that Borneo underwent kilometer-scale uplift and denudation during the last 20 Ma (e.g. Wilson et al., 1999; Hutchison et al., 2000; Hall and van Hattum, 2010). Paleomagnetic data show that the island did not significantly change its latitude during that period of time (e.g. Hall and van Hattum, 2010). Fig. 4a summarizes pre-Pliocene paleogeography compiled by Wilson et al. (1999). Marine carbonate rocks are widely distributed, especially along the southeastern seaboard where corals, coralline algae, radiolaria, echinoids, Halimeda, benthic and planktonic foraminifera with age ranges of 55–5 Ma have been recorded (Wilson et al., 1999).

In Miocene times, east Borneo experienced a dramatic switch in the style of sedimentation from carbonate shelf formation to clastic deltaic deposition and progradation (Fig. 4b; Wilson and Moss, 1999). The age of this switch within the deltas and basins that surround Borneo is ~ 23–17 Ma (Wilson and Moss, 1999). Apatite and zircon fission track analyses are consistent with rapid Neogene exhumation in north and west Borneo (Moss and Chambers, 1999; Hutchison et al., 2000). Significantly, this exhumation

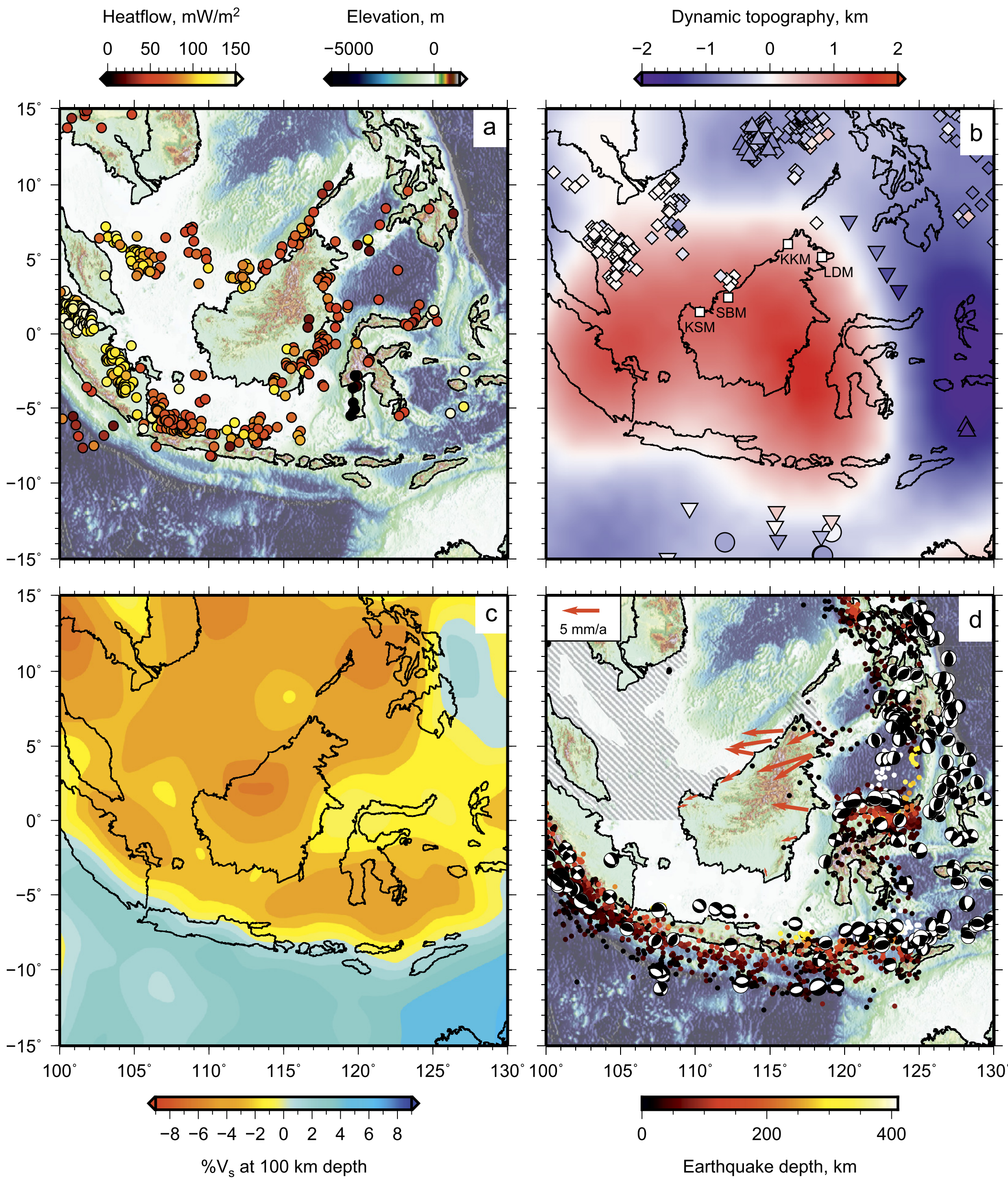

Fig. 2. (a) Topographic map of southeast Asia centered on Borneo. Colored circles = heatflow measurements from Southeast Asia Research Group (SEARG) catalog (e.g. Nagao and Uyeda, 1995). (b) Dynamic topography extracted from global spherical harmonic model ($l_{max} = 30$) generated using spot measurements of residual topography in the oceans and long wavelength ($\gtrsim$700 km) free-air gravity anomalies over continental lithosphere. Colored circles/upward- and downward-pointing triangles = estimates/lower and upper bounds of residual bathymetric anomalies in 1° bins (Hoggard et al., 2016). Labeled squares = broadband seismometer stations where crustal thicknesses were determined by receiver function analysis (27 ± 2 km at KSM; poorly determined at SBM; 27 ± 3 km at KKM; 33 ± 2 km at LDM; Lipke, 2008). (c) Horizontal slice through shear wave tomographic model at depth of 100 km (Schaeffer and Lebedev, 2013). (d) Earthquake seismicity between 1973 and 2016 from CMT catalog (Ekström et al., 2012). Colored circles = hypocentral depths; beach balls = earthquake focal mechanisms ($M_W > 6.5$); red arrows = GPS velocities with respect to Sunda Shelf (Simons et al., 2007; Mustafar et al., 2017); cross-hatched region = portions of Sunda Shelf (i.e. Sundaland) with bathymetry of < 50 m where continental crust is 29 ± 1 km thick (www.earthbyte.org; Holt, 2016).

is coeval with increased clastic flux and a concomitant reduction in carbonate production within these basins (Moss and Chambers, 1999; Hall and Nichols, 2002; Morley and Back, 2008). Hall and Nichols (2002) suggest that > 8 km of Neogene sediments were deposited in the basins surrounding Borneo. Unconformable surfaces offshore northern Borneo indicate that Middle Miocene uplift occurred over tens to hundreds of kilometers (Cullen, 2010). In southern Borneo, drainage developed on top of an incised warped peneplain (Figs. 4 and 5). Together, these stratigraphic and geomorphic observations imply that Borneo was uplifted and eroded during the last 20 Ma.

There is an excellent record of coeval magmatism (Fig. 4c and d). Peaks in magmatism occur at 22 ± 3 Ma and at 10 Ma. Whole rock K–Ar dates suggest that an early phase of calc-alkaline volcanism occurred in Eocene–Miocene times (e.g. Soeria-Atmadja et al., 1999). Late Miocene–Pleistocene basaltic lava flows crop out in the Sabah province of northeast Borneo. These rocks have high MgO numbers with the most mafic rocks containing nearly 8 wt% of MgO. Major and trace chemistry of samples from this region closely resembles ocean island basalts (Macpherson et al., 2010). Dioritic plutons occur on Mount Kinabalu (Soeria-Atmadja et al., 1999; Hall, 2009). Apatite and zircon fission track analyses have

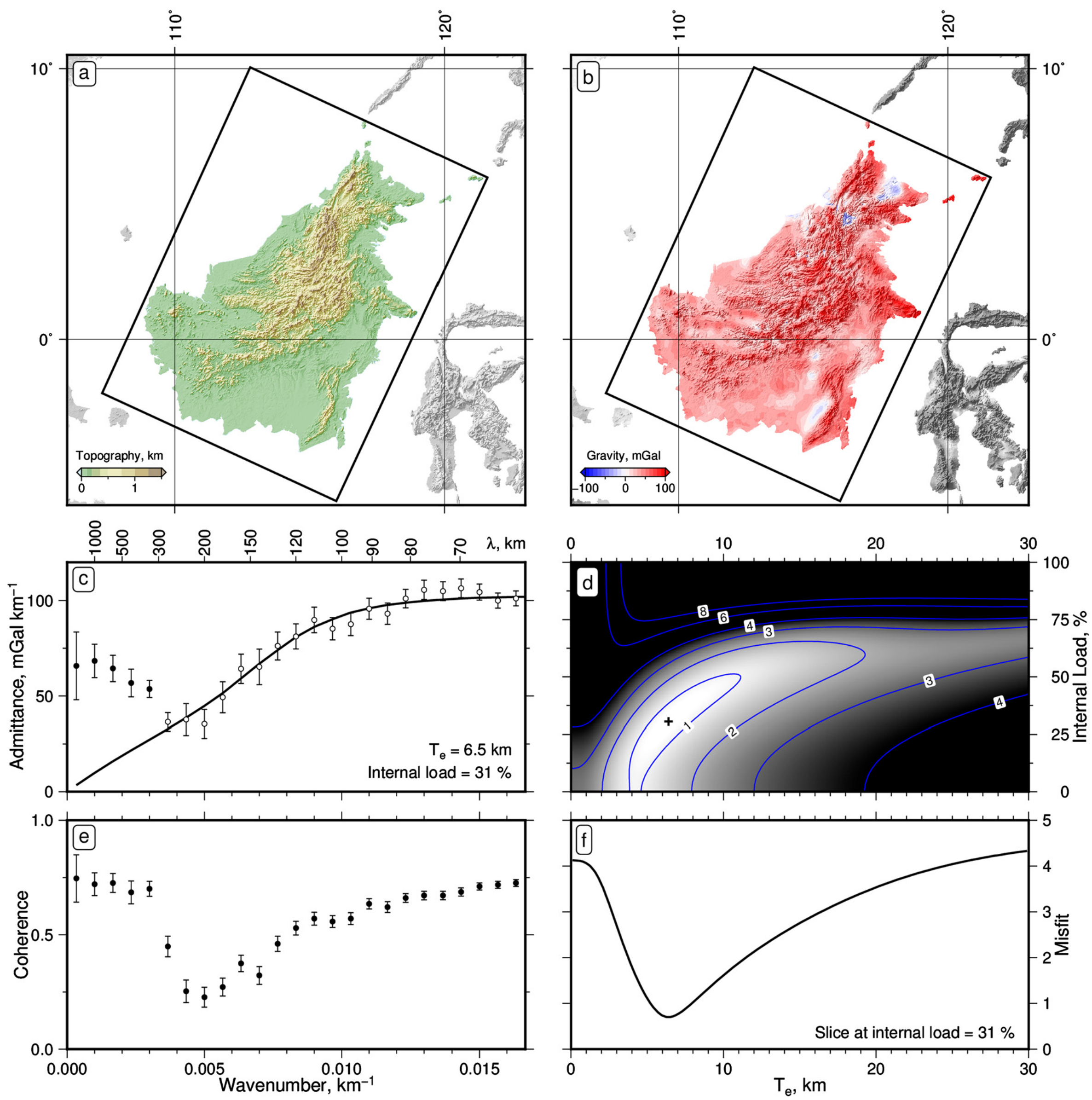

Fig. 3. (a) Topographic map of Borneo determined using SRTM_30_plus database (Becker et al., 2009). Box = region for which admittance analysis was carried out. (b) Free-air gravity map of Borneo determined using Eigen-6C_3stat database (Forste et al., 2012). (c) Admittance plotted as function of wavenumber. Open/solid circles with error bars = values of admittance determined by spectral analysis of topography and gravity; black line = admittance as function of wavenumber that best fits open circles for elastic thickness, $T_e = 7 \pm 3$ km; crustal thickness = 30 km; upper crustal thickness = 15 km; density of upper/lower crust = 2.45/2.9 $\mathrm{Mg\,m^{-3}}$, respectively. (d) Contoured rms misfit between observed and calculated admittance as function of elastic thickness, T_e, and percentage of internal load. Cross = locus of global minimum. (e) Coherence between topography and gravity as function of wavenumber. (f) Vertical slice through misfit function shown in panel (d) with global minimum at $T_e = 7 \pm 3$ km for internal load of 31%.

cooling histories that imply this pluton was exhumed during Late Miocene times (Cottam et al., 2013).

2.3. Isostatic considerations

Although Borneo sits within the Sundaland block at some distance from active plate boundaries, it has been suggested that youthful structural inversion and crustal thickening has played a role in generating and maintaining regional uplift (e.g. Morley et al., 2003; Franke et al., 2008). For example, the existence of local tectonic shortening has been invoked to help reconcile the present-day regional topography with global dynamic topographic models that predict regional draw-down (Spasojevic and Gurnis, 2012; Yang et al., 2016). To determine the extent to which Neogene plate shortening has played a role, we can explore its isostatic consequences, adapting the analysis of McKenzie (1978). If a reference column of continental lithosphere is shortened uniformly by a thickening factor, f, then the amount of regional uplift is given by

$$U = \frac{a\left[(\rho_m - \rho_c)\frac{t_c}{a}\left(1 - \frac{\alpha T_1}{2}\frac{t_c}{a}\right) - \frac{\alpha T_1}{2}\rho_m\right]}{\rho_m(1 - \alpha T_1)}(f - 1) \tag{1}$$

where values of the different symbols are given in Table 1 (see page 27 of McKenzie, 1978 for derivation of this equation). Significant portions of the Sundaland block that encompasses Borneo sit at, or very close to, sea level (Fig. 2d). Gravity modeling and basin analysis suggests that the average crustal thickness beneath this block is 29 ± 1 km and that the thermal time constant of post-rift subsidence observed within minor extensional sedimentary basins

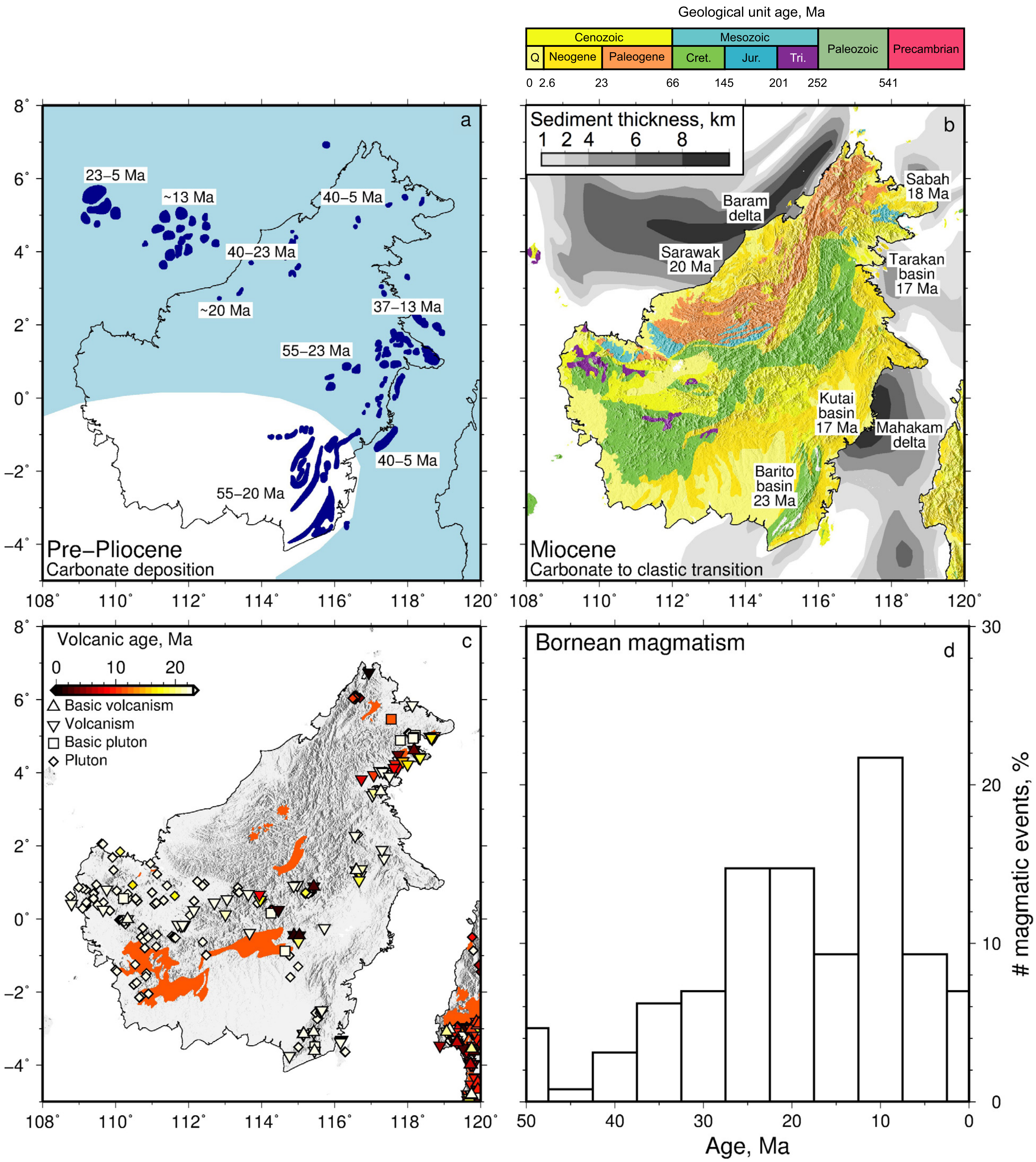

Fig. 4. (a) Pre-Pliocene paleogeography of region encompassing Borneo. Dark blue polygons = loci of Cenozoic marine carbonate deposits (Wilson et al., 1999). Light blue shading = distribution of Late Eocene marine conditions (Hall, 2009). (b) Miocene–Recent paleogeography. Colored units and bar = Mesozoic and Cenozoic stratigraphy (Choubert and Faure-Muret, 1976). Numbered labels = ages of transition from carbonate to clastic deposition (Wilson and Moss, 1999); gray isopachs = thickness of Cenozoic sedimentary deposits (Hall and Nichols, 2002). (c) Temporal and spatial distribution of magmatism from SEARG catalog (e.g. Moss et al., 1998; Macpherson et al., 2010). Orange polygons = basaltic igneous rocks (Choubert and Faure-Muret, 1976); triangles/squares/diamonds = intrusive/extrusive igneous rocks as indicated. (d) Histogram of Bornean magmatism taken from SEARG catalogue.

is consistent with a lithospheric thickness of $O(120)$ km (Holt, 2016). Therefore it is reasonable to assume for the purposes of our analysis that the thicknesses of crust and lithosphere, which yields zero elevation with respect to the mid-oceanic ridge, are $t_c = 30$ km and $a = 125$ km, respectively. If we assume a linear geothermal gradient, substitution of the values given in Table 1 yields

$$U = 2.1(f - 1) \qquad (2)$$

In order to generate 1 km of regional topography by lithospheric shortening, we require a thickening factor of $f = 1.5$, which yields a modern crustal thickness of 45 km. If northern Borneo is ~ 400 km across, its pre-shortened width is predicted to be 600 km. Assuming that lithospheric shortening occurred during the last 20 Ma yields an average convergence rate of 10 mm a^{-1}. The Global Positioning System (GPS) measurements of Mustafar et al. (2017) show that the present-day rate of horizontal shortening across northern Borneo between 3° and 7° N is minor and

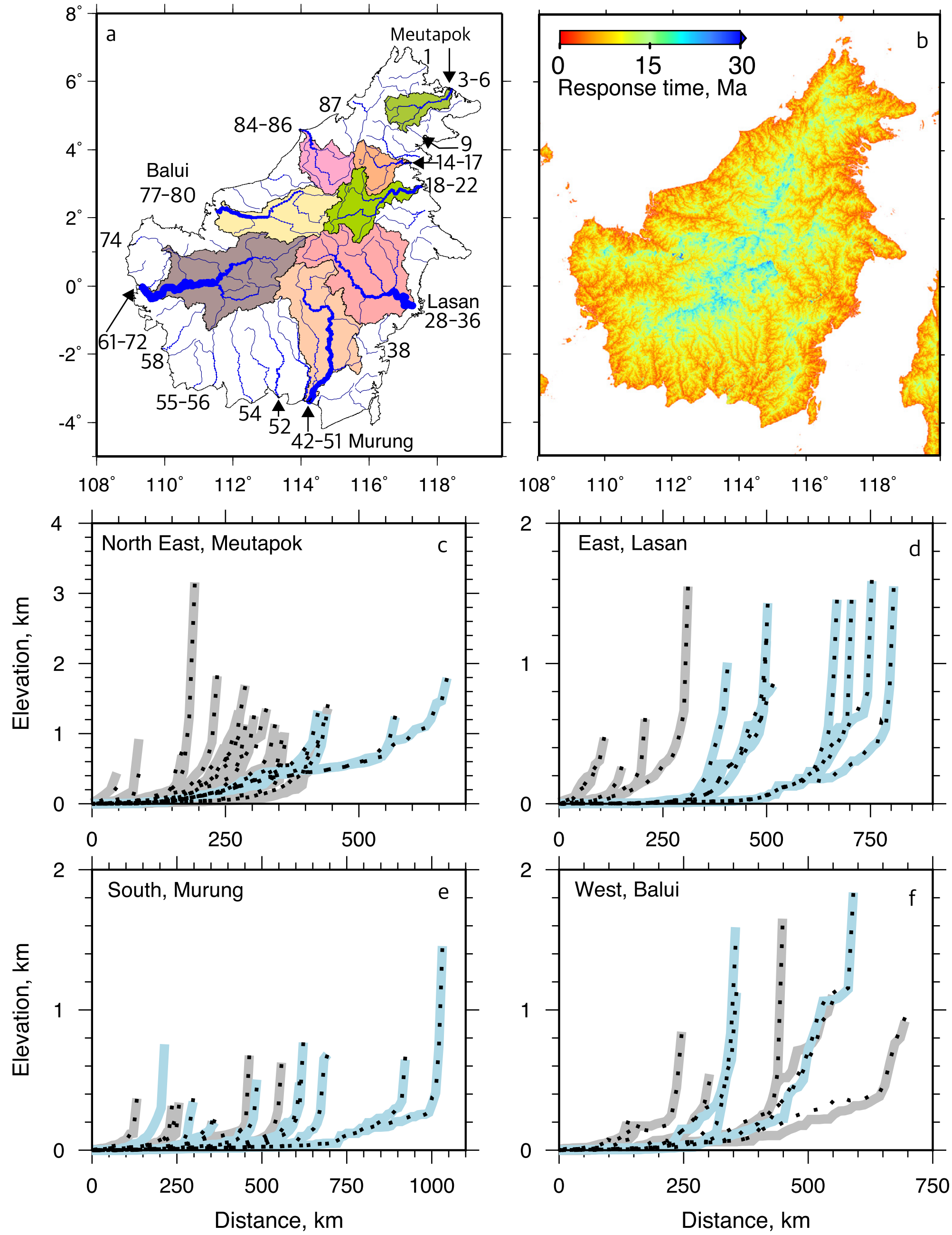

Fig. 5. (a) Extracted drainage network and major catchments. Blue lines = major rivers where line thickness is scaled according to upstream area (thickest lines = drainage areas $> 75 \times 10^3$ km^2); colored polygons = major catchments; numbers identify individual rivers from drainage inventory (Appendix A). (b) Landscape response time, τ_G, where $m = 0.5$ and $v = 0.7$ Ma^{-1}. (c) Gray lines = observed longitudinal profiles of rivers draining northeastern region (labeled 1–22 in panel (a) and Appendix A). Blue = Meutapok river and major tributaries. Dotted lines = best-fitting theoretical river profiles generated from inverse model shown in Fig. 6. (d) River profiles from eastern region, including Lasan catchment (23–36) (e) Southern region, including Murung catchment (42–58). (f) Western region, including Balui catchment (77–86). Global residual rms misfit = 1.61.

no more than 1–5 mm a^{-1} (Fig. 2d). This value corresponds to $f = 1.05$–1.1, which suggests that no more than $U = 100$–200 m of regional uplift is attributable to horizontal shortening across this region. We acknowledge that the rate of horizontal shortening in the past may have been different. This simplified analysis is consistent with the results of seismic wide-angle experiments and receiver function analyses, which suggest that the crust beneath northern Borneo and the adjacent continental shelf does not exceed 35 km (Fig. 2b; Franke et al., 2008; Lipke, 2008; Tang and Zheng, 2013). Nonetheless, we note that the highest Bornean topography that encompasses Mount Kinabalu is probably supported by local crustal thicknesses of 40 km or more (Holt, 2016). Elevated regional heatflow measurements are consistent with a general lack of lithospheric thickening. Instead, these measurements can be accounted for by anomalously high mantle temperatures (Fig. 2a). Fig. 2d confirms that active seismicity is concentrated at plate boundaries and that earthquake magnitudes on Borneo have not exceeded $M_W = 5.5$ since 1973. Together, these disparate observations imply that crustal thickening has not played an exclusive role in generating and maintaining present-day Bornean topography.

3. Geomorphic analysis

Spot measurements provide important constraints for landscape evolution. It is also illuminating to explore how these constraints can be combined with a fluvial geomorphologic under-

Table 1
Symbols and values of parameters.

Symbol	Parameter	Value
U	Regional uplift	km
D	Regional denudation	km
a	Lithospheric thickness	125 km
t_c	Crustal thickness	30 km
ρ_w	Density of water	$1\ \mathrm{Mg\,m^{-3}}$
ρ_s	Density of sediment	$2.4\ \mathrm{Mg\,m^{-3}}$
ρ_c	Density of crust (at 0 °C)	$2.8\ \mathrm{Mg\,m^{-3}}$
ρ_m	Density of lithospheric mantle (at 0 °C)	$3.33\ \mathrm{Mg\,m^{-3}}$
ρ_a	Density of asthenosphere	$3.2\ \mathrm{Mg\,m^{-3}}$
α	Thermal expansion coefficient	$3.28 \times 10^{-5}\,{}^\circ\mathrm{C}^{-1}$
T_1	Asthenospheric temperature	1333 °C
m	Empirical constant	$-2.8 \times 10^{-1}\ \mathrm{m\,s^{-1}} \oint \mathrm{C}^{-1}$
b_v	Empirical constant	$3.84 \times 10^{-4}\ \mathrm{km^{-1}}$
c	Empirical constant	$4720\ \mathrm{m\,s^{-1}}$
A	Empirical constant	$-1.8 \times 10^{16}\ \mathrm{m\,s^{-1}}$
E	Activation energy	$409 \times 10^{3}\ \mathrm{J\,mol^{-1}}$
V_a	Activation volume	$10 \times 10^{-6}\ \mathrm{m^3\,mol^{-1}}$
R	Gas constant	$8.3145\ \mathrm{J\,K^{-1}\,mol^{-1}}$

standing to calculate regional uplift histories. Roberts and White (2010) showed that individual longitudinal river profiles can be inverted to determine uplift rate as a function of time. Subsequently, Roberts et al. (2012) generalized this approach to allow large inventories of river profiles to be simultaneously inverted to determine uplift rate as a function of time and space.

Here, we seek a calibrated regional uplift history of Borneo in which inverse modeling of river profiles is combined with independent geomorphic, geologic and geophysical constraints. Our strategy is divided into three stages. First, we extract and check drainage networks. Secondly, we invert an island-wide inventory of river profiles. Thirdly, we test the calculated uplift history with a combination of onshore and offshore observations.

3.1. Drainage inventory

90 rivers were extracted from the 3 arc second (i.e. $\sim 90 \times 90$ m) Shuttle Radar Topography Mission (SRTM) database using standard flow-routing algorithms. The vertical accuracy of the SRTM dataset is ~ 20 m away from narrow and deep gorges. The fidelity and accuracy of the extracted drainage network was checked with Landsat imagery. We sought an even spatial distribution of river channels by extracting those with a Strahler order of greater than 3. The Bornean drainage inventory is summarized in Appendix A.

Fig. 5 summarizes the distribution of extracted river profiles, the planform of major catchments and the landscape response time. The drainage network has a strikingly radial pattern that is draped around the central highlands which coincide with a large positive free-air gravity anomaly. These highlands are drained by 7 major catchments, the largest of which are the Lasan, Murung and Kutungai river basins.

A summit envelope was reconstructed by draping a smooth surface across the principal drainage divides that are shown in Fig. 5a. The difference between this surface and the present-day landscape is a crude measure of the total volume of eroded material, $\Delta_v = 7.2 \times 10^5$ km^3. Borneo has a land area of $A_c = 7.3 \times 10^5$ km^2 and so the average elevation difference between the summit envelope and the present-day topography, $\overline{\Delta z} \approx 1$ km. If we allow for a post-Miocene sea-level decrease of 100 m and exclude topography below this elevation, $\Delta_v = 6.9 \times 10^5$ km^3, $A_c = 3.6 \times 10^5$ km^2 and $\overline{\Delta z} \approx 2$ km.

3.2. Inverse modeling strategy

One version of the empirical stream-power relationship that is used to calculate how river profiles evolve is given by

$$\frac{\partial z}{\partial t} = -vA(x)^m \frac{\partial z}{\partial x} + U(x,t), \tag{3}$$

where z is elevation, t is time, x is distance from the head of a river, A is upstream drainage area. v and m are erosional parameters whose values determine how rapidly a given landscape can evolve. Here, we assume that the slope exponent, n, has a value of 1. This assumption has been justified by Paul et al. (2014) who showed that misfit between observed and calculated river profiles has a global minimum located at $n \sim 1$. We acknowledge that on the shortest time and length scales, shock wave behavior may occur which would be consistent with $n > 1$.

The partial differential equation cannot easily be analytically solved unless an unrealistic steady-state assumption is made (i.e. $\partial z/\partial t = 0$). Building upon a suggestion of Whipple and Tucker (1999), Roberts et al. (2012) showed that a landscape response time, τ_G, could be calculated for a given eroding landscape where

$$\tau_G = \int_0^x \frac{\mathrm{d}x}{vA(x)^m}. \tag{4}$$

Fig. 5b shows the spatial variation of τ_G for Borneo when $v = 0.7$ Ma^{-1} and $m = 0.5$. This map shows how long it takes for an uplift signal inserted at the coastline to propagate through the landscape. Thus τ_G is a measure of the potential length of the 'tape recorder'. The oldest values are ~ 30 Ma, which suggests that the drainage network can potentially recover Neogene uplift signals. We are reluctant to place any interpretation on disparities in values of τ_G or similar parameters at drainage divides since the presence or absence of such disparities strongly depends upon the spatial pattern of inserted uplift (*contra* Willett et al., 2014).

Here, we attempt to extract an uplift rate history from the suite of river profiles. Observed river profiles are either convex-upward or concave-upward (e.g. Balui and Kutungai catchments, respectively; Fig. 5). Convex-upward profiles usually have knickzones that are 50–100 km wide and 0.5–1 km high. Concave-upward profiles have shorter wavelength knickpoints that probably reflect lithologic changes. Previous studies have shown that the spatial and temporal variation of regional uplift rate, U, can be determined by inverting observed river profiles (e.g. Pritchard et al., 2009; Roberts and White, 2010; Roberts et al., 2012; Rudge et al., 2015). If uplift rate is permitted to vary smoothly, a simplified version of the stream-power relationship can be used to match observed and calculated river profiles on a continent-wide basis (e.g. Paul et al., 2014). An ability to fit large inventories of river profiles is encouraging since it suggests that eroding landscapes contain interpretable signals that reflect their history of vertical motions.

Building upon previous optimization approaches, Rudge et al. (2015) showed that the linearized problem can be posed and solved without requiring a starting model that assumes *a priori* knowledge of the uplift history (Goren et al., 2014). One benefit of exploiting a damped linearized approach is that time taken to converge to a solution is one order of magnitude shorter than for non-linear optimization methods (e.g. Roberts and White, 2010; Roberts et al., 2012). This general approach attributes systematic long-wavelength changes in slopes along river profiles (i.e. knickzones) to smoothly varying uplift and erosion rate histories (see, e.g., Rudge et al., 2015). Subsequent approaches have been used to constrain uplift histories of modern and ancient landscapes (e.g. Roberts et al., 2012).

Our inverse modeling approach does not explicitly include the effects of variable precipitation. We recognize that fluctuations in precipitation with periodicities of tens of millions of years can shift calculated uplift histories. Shorter period (i.e. < 1 Ma) fluctuations have an almost negligible effect on resultant uplift rate histories (Paul et al., 2014). Changes in precipitation (i.e. discharge) on, for example, orbital-forcing timescales do not affect long wavelength shapes of calculated river profiles since the solution to Equation (1) is an integral. Thus average precipitation and discharge, on timescales of millions of years, seem to be of greater importance when solving for regional uplift rate histories. A significant corollary is that it may not be strictly necessary to have detailed knowledge of precipitation rates on geologic timescales to recover smooth uplift histories.

Our inverse model does not attempt to fit short wavelength knickpoints along river profiles. Significant spectral power along any river profile occurs on wavelengths > 10 km (Roberts and White, 2017). Thus, from a signal processing perspective, river profiles are spectrally red and short wavelength features (e.g. lithologic changes) might not have a significant influence upon the overall shape of a profile. This perspective is borne out by examining the relationship between riverbed lithology and profile slope or curvature, which do not appear to correlate when continent-wide inventories of river profiles are analyzed (e.g. Paul et al., 2014). For inverse modeling, our starting assumption is that all river profiles grade to a fixed reference level. Since the amplitude of glacio-eustatic sea-level variation is of order 10–100 meters, which is nearly one order of magnitude smaller than the amplitude of regional uplift considered here, the resultant short period fluctuations in reference level have a barely discernible effect upon our results (see, for example, Miller et al., 2005).

We have simultaneously inverted 90 river profiles to determine a smooth spatial and temporal history of uplift using a non-negative least squares (NNLS) inverse algorithm with spatial and temporal damping (Rudge et al., 2015; Fig. 5). In this algorithm, uplift rate is permitted to vary at vertices within an unstructured triangular grid (Fig. 6a). Uplift along each river profile is interpolated from surrounding vertices. It is important to emphasise two significant features of this inverse algorithm. First, no *a priori* assumptions are made about the spatial or temporal pattern of uplift since the starting model is the null set. Secondly, although the NNLS problem is solved using a limited memory version of the Broyden–Fletcher–Goldfarb–Shanno algorithm, which is appropriate when large sparse matrices feature, this pragmatic approach was carefully benchmarked by implementing the computationally slower active set algorithm of Lawson and Hanson (1987). This algorithm always converges optimally since it fulfils the Karush–Kuhn–Tucker conditions. We invert the matrix equation $\mathbf{z} = M\mathbf{U}$, and minimize

$$|M\mathbf{U} - \mathbf{z}|^2 + \lambda_S^2 |S\mathbf{U}|^2 + \lambda_T^2 |T\mathbf{U}|^2, \qquad \text{subject to} \quad \mathbf{U} \geq 0, \qquad (5)$$

to find uplift history $\mathbf{U}$, where $\mathbf{z}$ are the set of elevations along the river profiles (Rudge et al., 2015). The matrices S and T represent spatial and temporal smoothing, respectively. Smoothing parameters λ_S and λ_T control the regularization of this problem.

3.3. Inverse modeling results

We determine an uplift rate history that varies smoothly in space and time (Fig. 6a). This history yields a residual rms misfit of 1.61 between observed and calculated river profiles (Fig. 5). Nullity plots of model coverage are calculated to show that the best resolved component of the recovered uplift history is within the last 10 Ma. Model coverage is low before ~ 20 Ma (Fig. 6b). Calculated cumulative uplift is highest in northern Borneo with maximum uplift rates of 0.5–1 mm a^{-1} at ~ 5 Ma. In the northern ranges, maximum cumulative uplift occurs toward the west. The present-day calculated cumulative uplift and observed topography are well matched.

Calculated uplift histories depend upon the values of the erosional parameters, v and m and upon the degree of spatial and temporal damping applied to $U(x, y, t)$. The value of v sets the pace of fluvial erosion and we have chosen $v = 0.7$ Ma^{-1} to ensure that the start of regional uplift post-dates the youngest marine deposition observed onshore (Fig. 4). The chosen value of v can be independently tested by comparing the calculated uplift history with independent geologic measurements. The optimal value of m is determined by running a systematic suite of separate inverse models for the range $m = 0$–1 (Fig. 6d). This objective approach suggests that $m = 0.5 \pm 0.1$. Note that large uncertainties in the uplift drainage area, A, for each river profile has little impact upon our results because A is taken to a fractional power which acts to collapse error.

Finally, the recovered uplift history is generally dependent upon the values of the spatial and temporal damping parameters, λ_s and λ_t. In choosing the values of these parameters, we are guided by the strategy of Parker (1992) whereby the smoothest distribution of uplift that yields the smallest misfit is identified by running a set of inverse models for different values of λ_s and λ_t. For Borneo, it transpires that changes in λ_s have a much greater impact than changes in λ_t which was set at zero. λ_s was systematically varied to identify the locus of a subset of models that yields the smoothest uplift rate history which has the smallest residual misfit (i.e. $\lambda = 0.1$; Fig. 6c). We acknowledge that m and λ_s positively trade off against each other to some extent. Thus, higher values of λ_s necessitate higher values of m.

4. Independent testing

The calculated cumulative uplift history shown in Fig. 6a suggests that Bornean topography grew rapidly within the last 15–20 Ma. This hypothesis can be tested by comparing uplift histories at different locations across Borneo with a suite of different proxies such as facies changes, magmatism and rock cooling observations (Fig. 7).

4.1. Stratigraphic observations

The offshore distribution of Cenozoic marine carbonate rocks show that Borneo experienced significant youthful uplift (see, e.g., Wilson et al., 1999). Pre-Neogene carbonate production was spatially extensive (Fig. 7a). A decrease in carbonate production during Miocene times can be attributed to increased land area and to clastic efflux (Moss and Wilson, 1998). For example, Miocene deltaic progradation in the Kutai basin was accompanied by an increased proportion of sand. This clastic material contains volcanic fragments from the Late Oligocene and Early Miocene Sintang volcanoes (Moss and Chambers, 1999). A rapid transition from carbonate- to clastic-dominated deposition is observed at Bornean margins and can generally be attributed to regional Neogene uplift and denudation (see review of Hall and Nichols, 2002).

The stratigraphy of northwest Borneo contains important clues about its history of regional uplift (see, e.g., Levell, 1987; Wilson et al., 1999; Cullen, 2010; Hutchison, 2010). Fig. 7g summarizes the Cenozoic stratigraphy of Sarawak, Brunei and Sabah (Morley and Back, 2008). The turbiditic West Crocker, Mulu and Kelalan Formations are intercalated by the shaly Temburong Formation, which has foraminiferal assemblages indicative of Early Oligocene to Early Miocene deposition (see, e.g., Hutchison, 2010, p. 257;

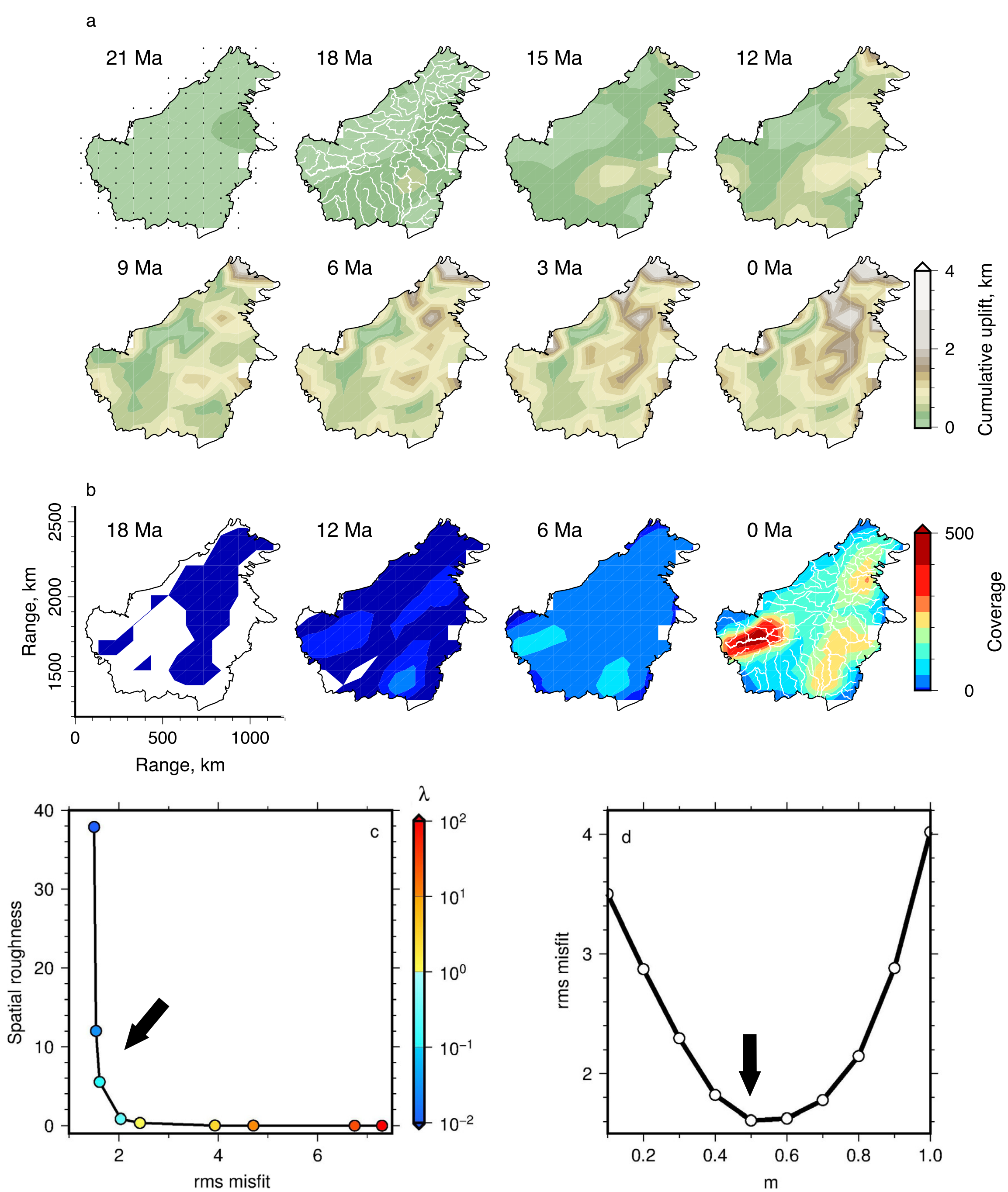

Fig. 6. (a) Calculated cumulative uplift history of Borneo. Solid circles = vertices at which uplift rate is calculated during inverse modeling. White lines = recovered drainage network used for inverse modeling. (b) Model coverage (nullity) plots showing number of non-zero entries in model matrix. (c) Residual rms misfit plotted as function of spatial smoothing, λ. Black arrow = locus of smoothest model that yields minimum misfit. (d) Residual rms misfit plotted as function of m. Black arrow = locus of global minimum at $m = 0.5$.

Cullen, 2010). Fossiliferous marine limestones of the Melinau Formation were deposited broadly contemporaneously across the southwestern region. This formation contains larger foraminifera (e.g. *Nummulites spp.*), fragmented corals, algae, echinoidal and bryzoan debris (Hutchison, 2010). Collectively, these observations indicate that extensive parts of northern Borneo were marine until ∼ 23 Ma. The Deep Regional Unconformity, observed on offshore seismic reflection profiles, separates these strata from the overlying Miocene to Recent Setap Shale and Belait Formations (Figs. 4b and 7g; Levell, 1987; Morley and Back, 2008; Cullen, 2010). The Late Oligocene to Late Miocene (11.6–5.3 Ma) Setap Shale Formation contains pelagic foraminifera (e.g. *Spiroclypeus sp.*, *Lepidocyclina sp.*, *Cycloclypeus sp.*; Hutchison, 2010). The presence of lignite within the clastic Belait Formation is suggestive of a Miocene–Pliocene transition to terrestrial conditions. The overlying Pliocene–Pleistocene Liang Formation contains sand, lignite and tuff (Hutchison, 2010). These observations imply that northern Borneo changed from a marine to terrestrial environment within the last ∼ 23 Ma. The Shallow Regional Unconformity (Late Miocene; ∼ 8 Ma) is mapped on offshore seismic reflection profiles from northern Borneo and its timing coincides with denudational unroofing of the Mount Kinabalu pluton, which has been constrained by apatite fission track analyses (Levell, 1987; Cullen, 2010; Cottam et al., 2013). It is likely that both of these regional unconformities

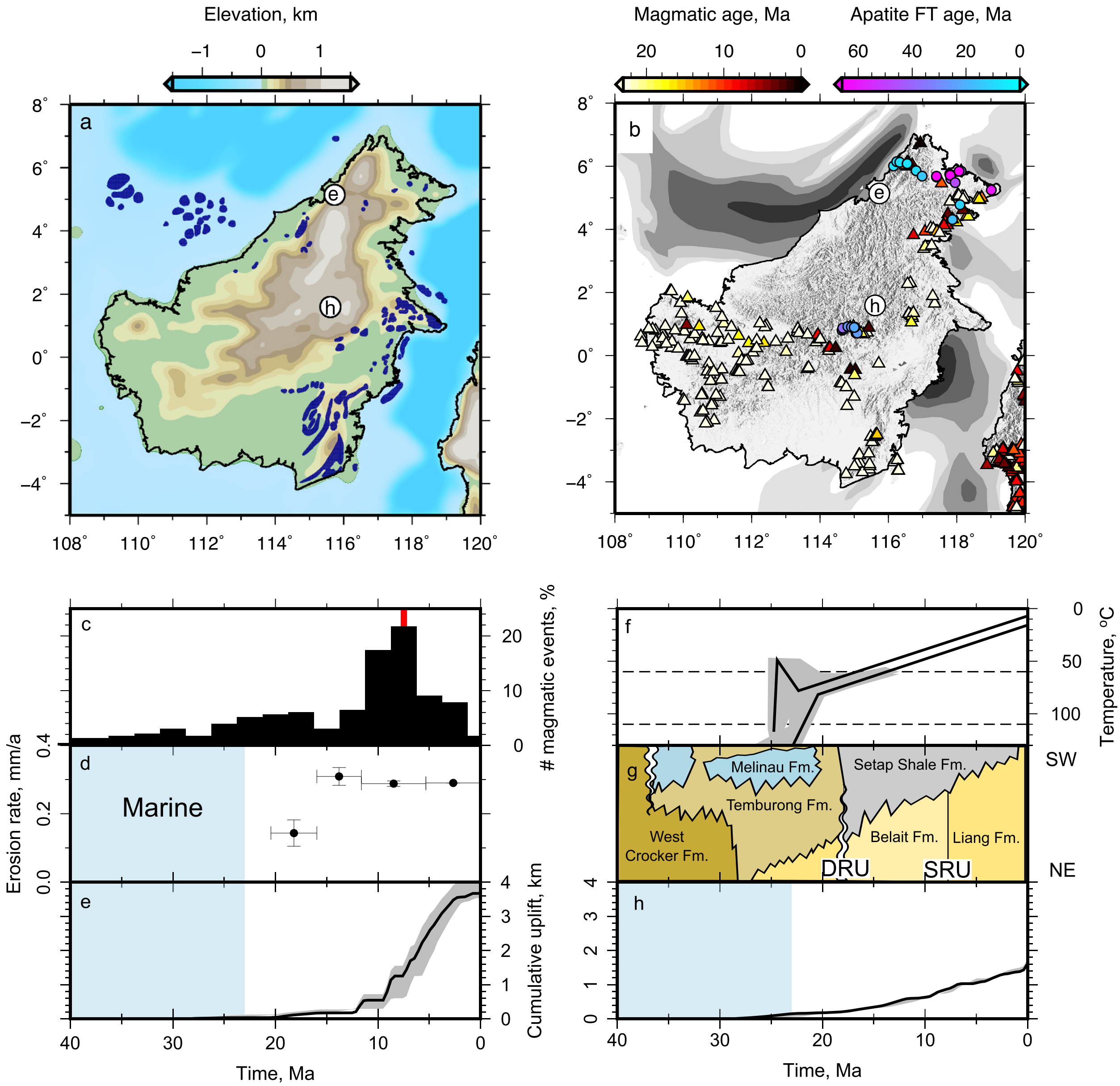

Fig. 7. (a) Long wavelength Bornean topography calculated from ETOPO1 database using Gaussian filter that is 100 km wide. Dark blue polygons = distribution of Oligocene–Neogene marine carbonate rocks (Wilson et al., 1999). Calculated cumulative uplift history is shown for labeled vertices in panels (e) and (h). (b) Magmatic, thermochronologic and depositional evidence. Gray shading = present-day topography; colored triangles = magmatism from SEARG catalogue (e.g. Macpherson et al., 2010); colored circles = apatite fission-track cooling ages (Moss et al., 1998; Hutchison et al., 2000; Cottam et al., 2013); contoured isopachs = offshore distribution of Neogene sedimentary rocks (scale shown on Fig. 5). (c) Histogram of magmatic events from SERG catalogue. Vertical red line = emplacement of Mount Kinabalu granite (Cottam et al., 2013). (d) Erosion rates determined from thermochronologic observations across northwest Borneo (Morley and Back, 2008). Light blue shading = marine conditions. (e) Calculated cumulative uplift at vertex shown in panel (a). Gray band = uncertainty for ±50% observed upstream drainage area. (f) Time–temperature histories determined from apatite fission track analyses of samples from central Borneo (Moss et al., 1998). (g) Stratigraphy for northern margin of Borneo (Morley and Back, 2008). West Crocker Formation: predominantly turbiditic sandstones and shales; Melinau Formation: marine biohermal limestone; Temburong Formation: argillaceous siltstones and shale; Meligan Formation: cross-bedded sandstone; Belait Formation: conglomerate and pebbly sandstones grading upward into fluvial to shallow marine sandstones, shales and coals; Liang Formation: clays, sandstone, lignites and tuffs (Hutchison, 2005). DRU/SRU = deep/shallow regional unconformities (Levell, 1987). (h) Calculated cumulative uplift histories at vertex shown in panel (a).

formed during uplift and tilting along the Bornean margin (Levell, 1987).

Building on Hamilton (1979)'s work, Hall and Nichols (2002) constructed maps of offshore sedimentary accumulation to constrain the timing and amplitude of Neogene denudation. Hall and Nichols (2002)'s map shows that sedimentary thicknesses exceed 8 km offshore Sarawak and Kutei where the most significant depocenters occur (Fig. 7b). Sedimentary accumulations offshore Tarakan and Sandakan are smaller but still exceed 6 km in thickness. The bulk of this sediment was deposited during Neogene times (Hall and Nichols, 2002). Hall and Nichols (2002) have used these offshore constraints to infer kilometer-scale Neogene denudation of the landmass. Morley and Back (2008) carried out a similar study of northwest Borneo and their results are summarized in Fig. 7d. Their measurements suggest that average erosion rates have been 0.1–0.3 mm a^{-1} since $\sim$20 Ma. Our inverse modeling results imply that hundreds meters of Neogene uplift of a region that includes the Schwaner Mountains of southwest Borneo occurred (Fig. 6). As a result, drainage networks of southern Borneo flow across a warped and incised peneplain of low relief that is a consequence of regional epeirogeny.

4.2. Thermochronology and magmatism

Cottam et al. (2013) reported zircon fission track (ZFT) ages of ∼5.5–7 Ma for a suite of samples taken from Mount Kinabalu, northern Borneo. If we assume that cooling was caused by denudation, we can estimate the amount of overburden that was removed. For example, if we follow Cottam et al. (2013) and assume a geothermal gradient of $25\,^{\circ}\mathrm{C\,km^{-1}}$, a surface temperature of 25 °C and a ZFT closure temperature of $205 \pm 18\,^{\circ}$C, we infer that more than 6 km of overburden was removed during the last ∼6 Ma. Cottam et al. (2013)'s apatite (U–Th–Sm)/He (AHe) ages are ∼1–10 Ma. Using their central age of 5.54 ± 0.08 Ma, an AHe closure temperature of 50–70 °C, and a surface temperature of 0–25 °C implies that 1–2.8 km of overburden was removed during the last ∼5.5 Ma. Thus, the calculated average Pliocene exhumation rates are fractions of a millimeter to millimeters per year. This exhumation history is broadly consistent with Hutchison et al. (2000)'s apatite fission track (AFT) ages of 6.7 ± 2.0 to 16.4 ± 1.9 Ma from the Western Cordillera and from the Labuk Highlands of northwestern Borneo. These fission track ages can be explained by removal of 3.4–4.4 km of overburden during the last ∼ 5–16 Ma, if we assume a closure temperature of 110–120 °C.

Overmature vitrinite reflectance measurements corroborate these observations (Hutchison et al., 2000; Hutchison, 2010: $R_{\circ} = 1.42 \pm 0.06\%$). Further east, the lowlands of Sabah have apatite fission track ages > 35 Ma (Hutchison et al., 2000). Moss et al. (1998) calculated time–temperature paths that best fit apatite fission ages and track lengths for a suite of samples collected along the Mahakam river in eastern Borneo. All of these samples have been reset (i.e. they were held at temperatures in excess of annealing temperatures since primary deposition). Modeled cooling histories indicate that exhumation of these sites occurred since ∼ 23 Ma with rapid rates of cooling at 23–20 Ma and more gradual cooling since (Fig. 7f). This denudation is broadly coeval with increased clastic input to the Mahakam Delta and with phases of magmatism (Fig. 7b; Moss et al., 1998).

Borneo is peppered by Cenozoic magmatism (Fig. 4c, e.g. Moss et al., 1998; Macpherson et al., 2010). Pre-Pliocene magmatism was predominantly calc-alkaline and therefore generated by subduction processes. Younger magmatism is generally less enriched (*cf.* e.g. Soeria-Atmadja et al., 1999; Macpherson et al., 2010). The number of Bornean magmatic events recorded in the SEARG catalog increases dramatically at ∼ 10 Ma. Pliocene–Pleistocene magmatism in the north of the island resembles ocean island basalts with MgO numbers up to 7.66 wt% (Macpherson et al., 2010).

5. Discussion

It has been predicted by most, but not all, dynamic topographic models that the bulk of southeast Asia from the Sea of Japan to the northern coast of Australia is convectively drawn down by more than 1 km (e.g. Lithgow-Bertolloni and Gurnis, 1997; Steinberger, 2007; Spasojevic and Gurnis, 2012; Yang and Gurnis, 2016). Borneo is positioned in the middle of this putative draw-down and yet it has an average elevation of ∼ 1 km. Here, we have exploited a combination of inverse modeling of a drainage inventory together with stratigraphic, thermochronologic, magmatic, and sedimentary efflux observations to propose that regional uplift of Borneo occurred within the last 20 Ma. Simple isostatic calculations combined with sparse crustal thickness and geodetic measurements imply that regional uplift is unlikely to be produced by crustal and lithospheric shortening alone. Beneath the Bornean lithosphere, there is significant evidence for a regionally extensive slow shear wave velocity anomaly at depths of 100–200 km (Fig. 1b). We acknowledge that an even more extensive fast shear wave velocity anomaly straddles the transition zone between the upper and lower mantle (Fig. 1d). Admittance analysis shows that at wavelengths of $O(10^3)$ km, $Z \geq +50\ \mathrm{mGal\,km^{-1}}$, which suggests that Bornean topography is supported by a mass deficit located somewhere within the upper mantle (Fig. 3).

There are two proposals that could account for the discrepancy between some geodynamic flow models and our reconstructed history of regional epeirogenic uplift. First, Bornean uplift could be attributed to a decrease in convective draw-down from, say, 3 to 2 km. Secondly, the amplitude and wavelength of convective draw-down may be incorrect and Bornean epeirogeny could have a much shallower origin. Significant problems preclude the first proposal. Convective draw-down of southeast Asia is thought to be generated by the presence of cold dense masses of subducted oceanic lithosphere that are visible on different tomographic models (e.g. Fig. 1d; Lithgow-Bertolloni and Gurnis, 1997). However, active subduction zones surrounding Borneo continue to contribute to this dense mass of cold slab material, suggesting that the putative convective draw-down is probably not shrinking. More significantly, Wheeler and White (2000) demonstrated that observed residual subsidence anomalies from fragments of oceanic crust throughout southeast Asia are inconsistent with large-scale draw-down. Borneo itself is bound to the east by fragments of oceanic lithosphere with residual depth anomalies that are up to −1 km (Fig. 2b). However, on the Sundaland block between Borneo and Indochina, Wheeler and White (2002) analyzed subsidence histories of extensional sedimentary basins and showed that residual subsidence anomalies are negligible to zero. Instead, the whole of the Sunda Shelf underwent modest regional uplift during Late Miocene times, which resulted in the development of an incised and lateritized peneplain that subsequently drowned during the Holocene transgression (Batchelor, 1979). Collectively, these observations suggest that inferred density anomalies within deeper parts of the mantle of southeast Asia have a nugatory influence on regional epeirogeny, which is dominated by uplift. Note that some recent dynamic topographic models that incorporate density anomalies within the upper mantle predict that a region encompassing Borneo is undergoing regional uplift (see, e.g., Yang et al., 2016; Steinberger et al., 2017; Müller et al., 2018).

Here, we investigate in more detail the second proposal, which focuses on shallower sub-plate density anomalies. Building upon the residual depth analysis of Wheeler and White (2000, 2002) and Hoggard et al. (2016) developed a spherical harmonic representation of a global database of observed present-day residual depth anomalies. Their global observations suggest that observed dynamic topography has significant short wavelength (e.g. $\sim 10^3$ km) components. This conclusion is borne out by examination of spot measurements of residual depth anomalies around Borneo (Fig. 2b). South of Borneo, amplitudes of observed anomalies decrease northward. In the South China Sea, negative anomalies of no more than −300 m are observed. These anomalies decrease southwestward toward the Sundaland block which has negligible anomalies. Borneo itself is characterized by a long wavelength positive gravity anomaly of 60 mGal that can be converted into a dynamic topography of 1 km, assuming an admittance of $Z \approx 60\ \mathrm{mGal\,km^{-1}}$. Hence a combination of spot measurements and gravity anomalies suggest that Borneo is the center of regional convective support that is probably maintained by thermally driven buoyancy anomalies within the uppermost mantle directly beneath the lithospheric plate.

The global tomographic model of Schaeffer and Lebedev (2013) shows that a significant slow shear wave anomaly occurs beneath a region that encompasses Borneo (Figs. 1b, 2c). Cross-

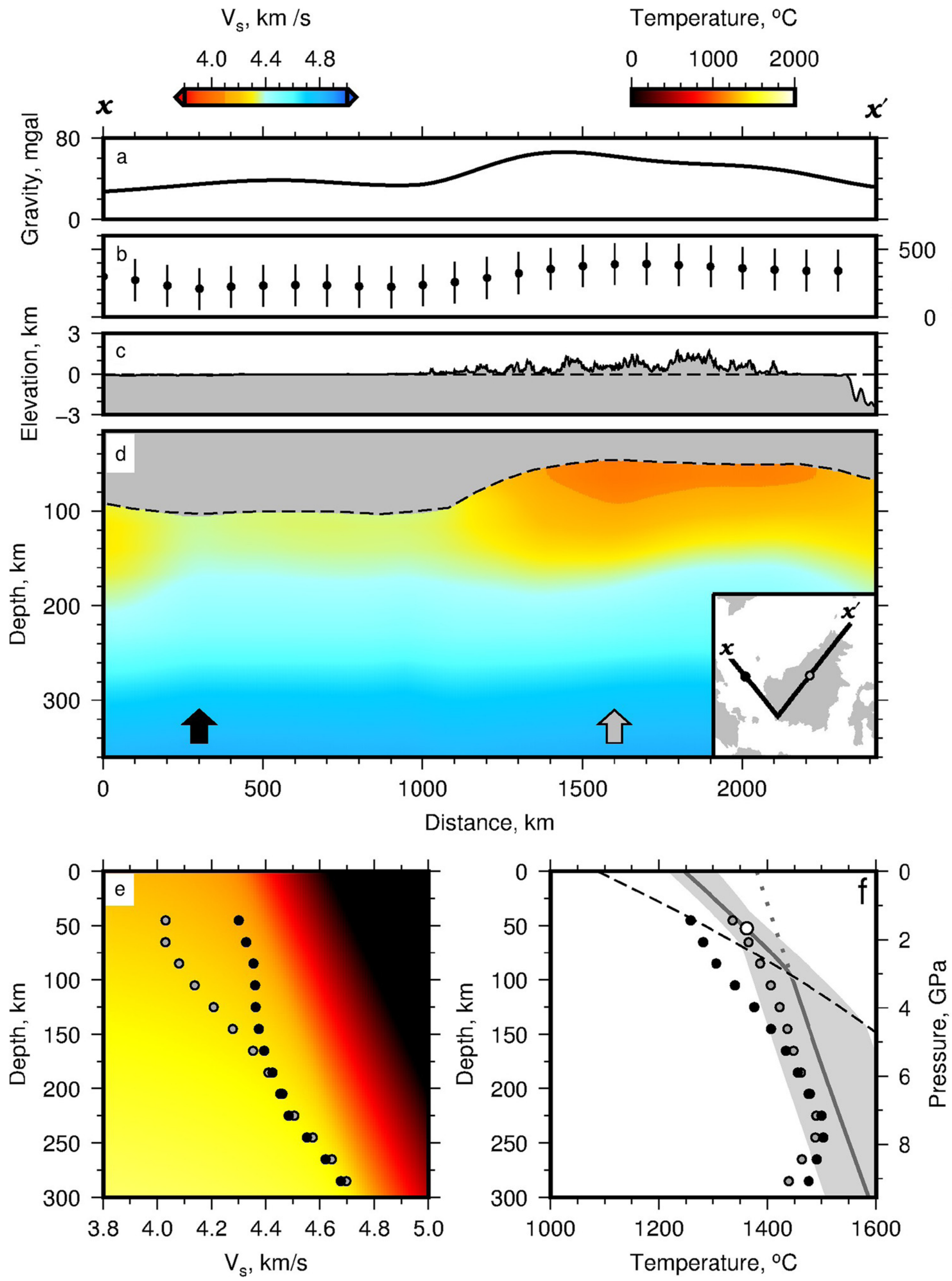

Fig. 8. Deep structure of Borneo. (a) NW-SE-NE transect, x–x', showing long wavelength (i.e. 700–2500 km) free-air gravity anomaly (location of transect shown in inset). (b) Uplift calculated along transect using sub-plate temperature variation determined by calibrating seismic tomographic model shown in panel (d). Solid circles with vertical bars = air-loaded uplift as function of distance, assuming that asthenosphere has ambient temperature of $1333 \pm 30\,^{\circ}$C. (c) Topographic height along transect. Dashed line = mean sea level. (d) Vertical slice through seismic tomographic model of Schaeffer and Lebedev (2013) converted into absolute velocity using their version of AK135 model. Gray polygon = regions where calculated temperature $<1333\,^{\circ}$C; dashed line = position of $1333\,^{\circ}$C isothermal surface. Gray/black arrows = loci of two calculated geothermal profiles shown in panels (d) and (e). (e) Contour map = temperature as a function of shear wave velocities, $V_s(z)$, and depth based on Priestley and McKenzie (2006)'s conversion scheme. Gray/black circles = $V_s(z)$ beneath central Borneo and Sunda Shelf, respectively (see arrows in panel d). (f) Pressure–temperature calculations. Gray/black circles = geothermal profiles beneath central Borneo and Sunda Shelf from V_s conversion scheme shown in panel (d). White circle = pressure and temperature estimates of primary melt for sample SBK13 with MgO number of 7.66 wt.% from Semporna peninsula (Macpherson et al., 2010). Pressures and temperatures were calculated using mafic thermobarometric method (Plank and Forsyth, 2016). Uncertainties in pressure and temperature estimates were determined for range of sample H_2O and Fe oxidation contents (McNab et al., 2018; see body text). Dotted line projected to surface indicates mantle potential temperatures ($T_p \approx 1380\,^{\circ}$C). Pressure–temperature estimates are compared to anhydrous melt paths (gray polygon) calculated using Katz et al. (2013)'s formulation. Dashed line is their anhydrous solidus.

sections through this and other tomographic models reveal that this anomaly is confined to a 150 ± 50 km thick layer, which sits immediately beneath the lithospheric plate. The correlation between this seismic anomaly and both topographic and free-air gravity anomalies is striking (Fig. 8a–d). The remaining issue is to determine whether or not this seismic anomaly represents a thermal perturbation that is sufficiently large to account for Bornean observations.

5.1. Asthenospheric temperature calibration

We investigate the possible link between observed shear wave velocity anomalies and regional uplift by converting Schaeffer and Lebedev (2013)'s model into temperature and then performing an isostatic calculation. Our strategy has three steps. First, we convert $\%V_s$ values reported by Schaeffer and Lebedev (2013) into absolute velocity using

$$V_s(z) = (\%V_s(z)/100)V_s^{\mathsf{AK135}}(z) + V_s^{\mathsf{AK135}}(z), \tag{6}$$

where z is depth and AK135 superscript refers to the relevant reference velocity model. Secondly, calculated values of $V_s(z)$ are converted into temperature using the approach of Priestley and McKenzie (2006). They suggested that a suitable empirical parametrization is $V_s = V_s(P, \Theta, a)$ where P is pressure, Θ is temperature in °C, and a is a variable that encapsulates the activation process. Their Equations (3) and (5) can be combined to give

$$V_s = \{1 + b_v(z - 50)\}\left\{m\Theta + c + A\exp\left(\frac{-E - PV_a}{RT}\right)\right\}, \tag{7}$$

where b_v, m, c, A, E and V_a are six empirical constants whose values and dimensions are given in Table 1. z is depth in km, T is temperature in Kelvin, and R is the gas constant. We assume that pressure is lithostatic such that $P = \rho g z$ where $\rho = 3.3$ Mg m^{-3} (i.e. $P \approx 30z$ MPa). To convert V_s into temperature, we use Equation (7) to generate a look-up chart which is shown on Fig. 8e.

Fig. 8d shows V_s as a function of range and depth for a transect that crosses the Sunda Shelf and Borneo. This transects shows that there is a discrete 100 km thick layer of slow shear wave velocities sitting directly beneath the lithospheric plate (i.e. $V_s =$ 4.0–4.4 km s^{-1}). Fig. 8e gives V_s as a function of depth beneath the Sunda Shelf and central Borneo at respective ranges of 300 and 1600 km along this transect. Using the empirical parametrization, we obtained an average temperature at a depth of 50–200 km of 1417 °C beneath Borneo (Fig. 8f). Between 1300 °C and 1500 °C at a depth of 150 km, a useful rule of thumb is

$$\Theta = 1500 - \exp(5.35V_s - 18.9), \tag{8}$$

where $V_s = 4.35$ km s^{-1} yields $\Theta = 1421$ °C. The validity of this estimate of asthenospheric temperature can be independently tested by using the major element geochemistry of basaltic igneous rocks to estimate melt equilibration temperature and pressure (Plank and Forsyth, 2016).

Here, we model elemental concentrations of the most mafic sample, SBK13, described by Macpherson et al. (2010). This sample has an MgO number of 7.66 ± 0.07 and is thought to have been derived by melting of an asthenospheric mantle source that was relatively uncontaminated by subduction zone processes. Uncertainties in estimates of the pressure and temperature of melt equilibration arise from the lack of direct observations of water content for this sample, of its iron oxidation content ($Fe^{3+}/\Sigma Fe$), and of the forsteritic content of mantle olivine. We have estimated water content using the Ce content of sample SBK13 by assuming a H_2O/Ce ratio of 200, which is consistent with estimates for depleted mantle and for the Pacific focal zone (Dixon et al., 2002). By using the relationship between V/Sc and oxidation state described by Lee et al. (2005), we obtain an estimate for $Fe^{3+}/\Sigma Fe$ of 0.17 for this single sample.

The resultant melt equilibration pressure and temperature estimates calculated by applying the thermobarometer of Plank and Forsyth (2016) are 1362 ± 39 °C and 1.66 ± 0.24 GPa (i.e. 55 ± 8 km), respectively. If we assume that this sample lies upon a melting path, the locus where this path crosses the dry solidus can be used to determine mantle potential temperature, T_p. Our pressure and temperature equilibration results are compared to the anhydrous melt paths of Katz et al. (2013). The path that lies closest to the sample point is used to estimate $T_p \approx 1380^{+100}_{-70}$ °C (i.e. ~ 50 °C hotter than ambient mantle temperatures).

In order to reconcile the major element geochemistry of sample SBK13 with an ambient mantle temperature would require H_2O/Ce and $Fe^{3+}/\Sigma Fe$ ratios that are significantly greater than those expected for ocean island basalt (OIB) melting. Therefore, our single result suggests that the asthenospheric mantle beneath northern Borneo is hotter than ambient mantle. It is important to bear in mind that this approach is limited by being restricted to a single sample with an MgO wt% value that is slightly less than 8 (note that the thermobarometric scheme does not account for fractionation of plagioclase or clinopyroxene). This qualification means that the calculated temperature could have been overestimated to some extent. However, by assuming that the mantle source is anhydrous and by discounting the effects of conductive cooling at the base of the lithosphere, a potential temperature of ~ 1380 °C is probably an underestimate (McNab et al., 2018). We conclude that a combination of a finite value of admittance at long wavelengths, slow shear wave velocities, and an estimate of melt equilibration temperature imply that the sub-plate asthenosphere is hotter than the ambient value of 1333 °C.

Finally, we revisit isostatic considerations. Previously, we showed that present-day rates of horizontal tectonic shortening are unlikely to account for the scale and amplitude of regional uplift. Other plausible mechanisms of regional uplift are emplacement of a layer of anomalously warm asthenosphere beneath the lithospheric plate and intrusion of magmatic underplating within the lower crust. Here, we estimate in turn the contribution that each of these mechanism can make. First, we calculate regional uplift as a function of temperature and thickness of a warm layer of asthenosphere using Equation (2) of Rudge et al. (2008) who showed that

$$U = \frac{2h\alpha\Delta T}{1 - \alpha T_\circ}, \tag{9}$$

where $2h$ is layer thickness, which we set to 150 km. Average excess temperature is ΔT, and $T_\circ$ is background temperature (see page 151 of Rudge et al., 2008). If the mean temperature of the mantle immediately beneath Borneo is 1417 °C and $T_\circ = 1333 \pm 30$ °C, $\Delta T = 84 \pm 30$ °C which yields an air-loaded uplift of 432 ± 154 m. This simple estimate suggests that a significant component of Bornean topography is supported by an anomalously warm layer of asthenosphere that was probably emplaced within the last 20 Ma.

Secondly, we calculate regional uplift as a function of the thickness and density of an intruded layer of magmatic underplating using Equation (1) of Brodie and White (1994) who showed that

$$U = (1 - \rho_x/\rho_a)\,x \tag{10}$$

where x and ρ_x are the thickness and density of magmatic underplating and $\rho_a = 3.2$ Mg m^{-3} is asthenospheric density (see page 149 of Brodie and White, 1994). In the absence of lithospheric thinning, a reasonable upper bound for the amount of magmatic underplating is $x = 5$ km for a density of $\rho_x = 2.9$ Mg m^{-3}, which yields $U = 469$ m.

In this way, we suggest that regional uplift of Borneo can be partitioned into three contributions. The first contribution is from regional tectonic shortening of the lithospheric plate. The present-day rate of shortening across northern Borneo is 1–5 mm yr^{-1} which by extrapolation yields 100–200 m of regional uplift over 20 Ma. The second contribution is from putative magmatic underplating associated with basaltic volcanism, which could yield as much as 500 m of sub-regional uplift focused beneath, say, Mount Kinabalu. The final contribution is from a warm layer of sub-plate asthenospheric mantle which yields regional uplift of up to 500 m beneath Borneo. The transect shown in Fig. 8d suggest that this warm layer extends beneath the Sunda Shelf where the average excess temperature is only $\Delta T \le 38 \pm 30$ °C. This value yields an air-loaded uplift of 196 ± 155 m, which is consistent with geomorphic evidence for fluvial incision and lateritization of an emergent peneplain during Late Miocene times (Batchelor, 1979). This peneplain was drowned during the Holocene transgression.

6. Conclusions

A suite of geodynamic flow models predict that an area encompassing Borneo and the adjacent Sunda Shelf is dynamically drawn down by 1–2 km. However, geophysical, geomorphic and geochemical data indicate that it is more likely that positive convective support has played a significant role in generated Bornean topography. Slow shear wave velocity anomalies directly beneath the Bornean lithosphere, positive long wavelength free-air gravity data and a mafic magmatic history are all indicative of up to 1 km of positive dynamic support. Conversion of shear velocities to temperature and simple isostatic calculations suggest that nearly 500 m of regional topography is maintained by a layer of anomalously warm asthenospheric mantle which sits directly beneath the Bornean lithosphere. The existence of this layer is consistent with the pressure and temperature of melting calculated using major element chemistry of basaltic rocks. Inverse modeling of the fluvial drainage network suggests that this sub-plate support probably grew during the last 20 Ma. We acknowledge that some combination of regional tectonic shortening and magmatic underplating could have generated an additional 0.5–0.7 km of regional uplift. Our results are corroborated by independent geologic observations (e.g. sedimentary flux, thermochronometry, carbonate and clastic sequences, basaltic magmatism) and have important implications for models that favor wholesale convective draw-down.

Acknowledgements

Magmatic and heat flow data can be downloaded from http://searg.rhul.ac.uk/. ASTER data can be downloaded from http://gdem.ersdac.jspacesystems.or.jp. SRTM data is available at http://www.cgiar-csi.org. Digital CGMW geologic maps can be downloaded from http://energy.usgs.gov. Earthquake catalogue is from http://www.globalcmt.org. We are grateful to D. McKenzie for generously providing the admittance code. We thank I. Frame, D. Lyness, F. Richards, S. Stephenson and J. Winterbourne for their help. J. Armitage and N. Flament wrote careful and exacting reviews that enabled us to clarify our arguments. Cambridge Earth Sciences contribution number esc.4289.

Appendix A. Drainage inventory

Table A.2 is an inventory of the rivers used in this study. Latitude and longitude of river heads, lengths, maximum drainage areas and elevations were calculated using the SRTM 3 arc-second dataset and Esri flow routing algorithms.

Table A.2
Drainage inventory for northeastern rivers.

#	Name	Catchment	Lat. (°)	Long. (°)	Length (km)	Area (km^2)	Elevation (km)
1	Sugut	A	117.67	6.43	193	3113	3.16
2	Labuk	A	117.46	5.88	235	4717	1.82
3	Meutapok	A	118.43	5.77	424	16081	0.78
4	Lokan	A			404	16068	0.68
5	Kinabantangan	A			355	16085	1
6	Kuamut	A			361	16079	1.02
7	Segama	A	118.73	5.43	263	3910	0.9
8	Magdalena	A	117.73	4.5	46	307	0.44
9	Cowie	A	117.53	4.37	88	1287	0.92
10	Sebuku	A			168	3162	0.69
11	Sembakung	A			352	10092	0.53
12	Witti	A			343	10092	1.13
13	Pensiangan	A			304	10092	1.25
14	Kabinu	A	117.15	3.62	287	15643	1.69
15	Pakerajan	A	117.21	3.62	275	15775	1.32
16	Murud	A			327	15643	1.35
17	Tubu	A			287	15806	1.13
18	Bahau	A	117.51	2.91	442	29766	1.36
19	Kajan	A			423	29812	1.33
20	Iwan	A			665	29812	1.79
21	Longuru	A			568	29765	1.24
22	Kajan	A			439	29812	1.28
23	Berau	B	117.62	2.21	208	14384	0.6
24	Longgi	B			311	14384	1.55
25	Niapa	B	118.02	1.74	109	1760	0.47
26	Baai	B	117.84	1.22	88	3501	0.28
27	Sepasu	B	117.71	0.7	151	3063	0.26
28	Telen	B	117.26	−0.57	503	75282	1.43
29	Longwai	B			405	75289	1.01
30	Belajan	B			499	75290	1.16
31	Len	B			516	75290	0.85
32	Lasan	B			753	75055	1.59
33	Mahakam	B			705	75055	1.46
34	Batubrok	B			669	75290	1.46
35	Nahabuan	B			806	75043	1.55
36	Balikpapan	B			378	75289	0.32
37	Sebakung	C	116.54	−1.54	180	3661	0.35
38	Besar	C	116.25	−1.91	160	3947	0.47
39	Besar	C			130	1468	0.67
40	Klumpeng	C			82	1914	0.51
41	Kukusang	C	115.9	−3.61	127	1559	0.42
42	Kandangan	D	114.51	−3.5	213	11521	0.76
43	Kapuas	D	114.26	−3.37	298	66564	0.35

Table A.2 (*continued*)

#	Name	Catchment	Lat. (°)	Long. (°)	Length (km)	Area (km^2)	Elevation (km)
44	Negara	D			362	66568	0.2
45	Tewe	D			611	66562	0.48
46	Barito	D			693	66560	0.68
47	Murung	D			1031	66564	1.46
48	Muaradjuloi	D			922	66520	0.65
49	Kualakapuas	D			485	66579	0.5
50	Kahajan	D	114.07	−3.33	622	17354	0.77
51	Rungan	D			439	17354	0.15
52	Mendawai	D	113.34	−3.26	558	19035	0.62
53	Sampit	D	113.03	−2.96	354	13292	0.2
54	Serujan	D	112.56	−3.4	463	12930	0.68
55	Sekima	D	111.43	−2.89	242	14073	0.2
56	Raja	D			256	14073	0.34
57	Matua	D	110.85	−2.99	236	6722	0.31
58	Pesaguan	D	110.14	−2.04	132	1626	0.37
59	Pawan	D	109.94	−1.84	315	10174	0.36
60	Djenu	D	109.76	−0.89	157	2848	0.38
61	Kotabaharu	E	109.39	−0.08	694	82820	0.26
62	Melawi	E			864	82901	0.92
63	Beturan	E			803	82814	0.21
64	Kajan	E			646	82820	0.8
65	Piabung	E			609	82851	0.35
66	Nangasuruk	E	109.35	−0.03	831	82909	0.57
67	Kualakeriau	E			921	82909	0.84
68	Tje Maru	E			1024	82901	1.18
69	Betung	E			919	82790	0.43
70	Kutungai	E			696	82909	0.28
71	Menkiang	E			476	82859	0.79
72	Landak	E			282	8187	0.76
73	Bengkajan	E	108.95	0.39	105	1659	0.48
74	Sambas	E	108.97	1.2	179	8082	0.6
75	Simunjan	E	110.69	1.25	68	1950	0.37
76	Lupar	E	111.33	1.34	108	4011	0.06
77	Katibas	F	111.56	2.19	302	42472	0.54
78	Baleh	F			449	42468	1.65
79	Balui	F			694	42472	0.92
80	Plieran	F			549	42472	1.11
81	Mukah	F	112	2.88	139	1724	0.14
82	Kakus	F	112.82	3.07	160	4830	0.19
83	Tubau	F	113.04	3.17	246	8676	0.85
84	Tinjar	F	113.98	4.58	356	22228	1.12
85	Baram	F			591	22227	1.84
86	Tutoh	F			354	22227	1.59
87	Trusan	G	115.31	4.89	172	2500	1.5
88	Padas	G	115.54	5.41	228	8803	1.45
89	Trus Madi	G			207	8813	0.83
90	Kalupis	G	116.21	6.17	59	967	1.54

References

Batchelor, B.C., 1979. Geological characteristics of certain coastal and offshore placers as essential guides for tin exploration in Sundaland, Southeast Asia. Geol. Soc. Malaysia Bull. 11, 283–313.

Becker, J.J., Sandwell, D.T., Smith, W.H.F., Braud, J., Binder, B., Depner, J., Fabre, D., Factor, J., Ingalls, S., Kim, S-H., Ladner, R., Marks, K., Nelson, S., Pharaoh, A., Trimmer, R., Von Rosenberg, J., Wallace, G., Weatherall, P., 2009. Global bathymetry and elevation data at 30 arc seconds resolution: SRTM30_PLUS. Mar. Geod. 4, 355–371. https://doi.org/10.1080/01490410903297766.

Brodie, J., White, N., 1994. Sedimentary basin inversion caused by igneous underplating: northwest European continental shelf. Geology 22, 147–150.

Choubert, G., Faure-Muret, A., 1976. Geological World Atlas. UNESCO, Paris.

Cottam, M.A., Hall, R., Sperber, C., Kohn, B.P., Forster, M.A., Batt, G.E., 2013. Neogene rock uplift and erosion in northern Borneo: evidence from the Kinabalu granite, Mount Kinabalu. Mem. Geol. Soc. Lond. 170, 805–815. https://doi.org/10.1144/jgs2011-130.

Cullen, A.B., 2010. Transverse segmentation of the Baram-Balabac basin, NW Borneo: refining the model of Borneo's tectonic evolution. Pet. Geosci. 16, 3–29. https://doi.org/10.1144/1354-079309-828.

Dixon, J.E., Leist, L., Langmuir, C., Schilling, J.-G., 2002. Recycled dehydrated lithosphere observed in plume-influenced mid-ocean-ridge basalt. Nature 420, 385–389.

Ekström, G., Nettles, M., Dziewonski, A.M., 2012. The global CMT project 2004–2010: centroid-moment tensors for 13,017 earthquakes. Phys. Earth Planet. Inter. 200–201, 1–9. https://doi.org/10.1016/j.pepi.2012.04.002.

Flament, N., Gurnis, M., Müller, R.D., 2013. A review of observations and models of dynamic topography. Lithosphere 5 (2), 189–210.

Forste, C., Bruinsma, S.L., Flechtner, F., Marty, J.-C., Lemoine, J.-M., Dahle, C., Abrikosov, O., Neumayer, K.H., Biancale, R., Barthelmes, F., Balmino, G., 2012. A preliminary update of the Direct approach GOCE Processing and a new release of EIGEN-6C. In: AGU Fall Meeting.

Franke, D., Barckhausen, U., Heyde, I., Tingay, M., Ramli, N., 2008. Seismic images of a collision zone offshore NW Sabah/Borneo. Mar. Pet. Geol. 25, 606–624.

Goren, L., Fox, M., Willett, S.D., 2014. Tectonics from fluvial topography using formal linear inversion: theory and applications to the Inyo Mountains, California. J. Geophys. Res., Earth Surf. 119. https://doi.org/10.1002/2014JF003079.

Hall, R., Nichols, G.J., 2002. Cenozoic sedimentation and tectonics in Borneo: climatic influences on orogenesis. In: Jones, S.J., Frostick, L. (Eds.), Sediment Flux to Basins: Causes, Controls and Consequences. In: Geol. Soc. (Lond.) Spec. Publ., vol. 191, pp. 5–22.

Hall, R., 2009. SE Asia's changing palaeogeography. Blumea 54, 148–161.

Hall, R., van Hattum, M.W.A., 2010. Impact of India–Asia collision on SE Asia: the record in Borneo. Tectonophysics 451, 366–389.

Hamilton, W.B., 1979. Tectonics of the Indonesian region. U. S. Geol. Surv. Prof. Pap. 1078.

Holt, R.A., 2016. The Gravity Field of Sundaland – Acquisition, Assessment and Interpretation. D. Phil. Diss., Uni. London.

Hoggard, M.J., White, N., Al-Attar, D., 2016. Global dynamic topography observations reveal limited influence of large-scale mantle flow. Nat. Geosci. 9. https://doi.org/10.1038/NGEO2709.
Hutchison, C.S., Bergman, S.C., Swauger, D.A., Graves, J.E., 2000. A Miocene collisional belt in north Borneo: uplift mechanism and isostatic adjustment quantified by thermochronometry. J. Geol. Soc., Lond. 157, 783–793.
Hutchison, C.S., 2005. Geology of North West Borneo: Sarawak, Brunei and Sabah. Elsevier, Netherlands.
Hutchison, C.S., 2010. The North-West Borneo Trough. Mar. Geol. 271, 32–43.
Katz, R.F., Spiegelman, M., Langmuir, C.H., 2013. A new parameterization of hydrous mantle melting. Geochem. Geophys. Geosyst. 4 (9). https://doi.org/10.1029/2002GC000433.
Lawson, C.L., Hanson, R.J., 1987. Solving Least Squares Problems. Prentice-Hall, New York.
Lee, C.-T.A., Leeman, W.P., Canil, D., Li, Z.-X.A., 2005. Similar V/Sc systematics in MORB and arc basalts: implications for the oxygen fugacities of their mantle source regions. J. Petrol. 46 (11), 2313–2336.
Levell, B.K., 1987. The nature and significance of regional unconformities in the hydrocarbon-bearing Neogene sequences offshore west Sabah. J. Geol. Soc. Malaysia Bull. 21, 55–90.
Lipke, 2008. Seismologic Investigation of the Sunda Arc Region with Receiver Functions. Dip. Th., Univ. Potsdam.
Lithgow-Bertolloni, C., Gurnis, M., 1997. Cenozoic subsidence and uplift of continents from time-varying dynamic topography. Geology 25, 735–738.
Macpherson, C.G., Chiang, K.K., Hall, R., Nowell, G.M., Castillo, P.R., Thirlwall, M.F., 2010. Plio-Pleistocene intra-plate magmatism from the southern Sulu Arc, Semporna peninsula, Sabah, Borneo: implications for high-Nb basalt in subduction zones. J. Volcanol. Geotherm. Res. 190, 25–38.
McKenzie, D., 1978. Some remarks on the development of sedimentary basins. Earth Planet. Sci. Lett. 40 (1), 25–32.
McKenzie, D., 2010. The influence of dynamically supported topography on estimates of T_e. Earth Planet. Sci. Lett. 295 (1–2), 127–138.
McNab, F., Ball, P.W., Hoggard, M.J., White, N.J., 2018. Neogene uplift and magmatism of Anatolia: insights from drainage analysis and basaltic geochemistry. Geochem. Geophys. Geosyst. https://doi.org/10.1002/2017GC007251.
Miller, K.G., Kominz, M.A., Browning, J.V., Wright, J.D., Mountain, G.S., Katz, M.E., Sugarman, P.J., Cramer, B.S., Christie-Blick, N., Pekar, S.F., 2005. The Phanerozoic record of global sea-level change. Science 310 (5752), 1293–1298.
Morley, C.K., Back, S., 2008. Estimating hinterland exhumation from late orogenic basin volume, NW Borneo. J. Geol. Soc., Lond. 165, 353–366.
Morley, C.K., Back, S., Van Rensbergen, P., Crevello, P., Lambiase, J.J., 2003. Characteristics of repeated, detached, Miocene–Pliocene tectonic inversion events, in a large delta province on an active margin, Brunei Darussalam, Borneo. J. Struct. Geol. 25, 1147–1169.
Moss, S.J., Wilson, M.E.J., 1998. Biogeographic implications of the Tertiary palaeogeographic evolution of Sulawesi and Borneo. In: Hall, R., Holloway, J.D. (Eds.), Biogeography and Geological Evolution of SE Asia. Blackhuys Publishers, Leiden, The Netherlands, pp. 133–163.
Moss, S.J., Carter, A., Baker, S., Hurford, A.J., 1998. A late Oligocene tectono-volcanic event in East Kalimantan and the implications for tectonics and sedimentation in Borneo. J. Geol. Soc., Lond. 155, 177–192.
Moss, S.J., Chambers, J.L.C., 1999. Tertiary facies architecture in the Kutai Basin, Kalimantan, Indonesia. J. Asian Earth Sci. 17, 157–181.
Müller, R.D., Hassan, R., Gurnis, M., Flament, N., Williams, S.E., 2018. Dynamic topography of passive continental margins and their hinterlands since the Cretaceous. Gondwana Res. 53, 225–251.
Mustafar, M.A., Simons, W.J.F., Tongkul, F., Satirapod, C., Omar, K.M., Visser, P.N.A.M., 2017. Quantifying deformation in North Borneo with GPS. J. Geod. 91, 1241–1259.
Nagao, T., Uyeda, S., 1995. Heat-flow distribution in Southeast Asia with consideration of volcanic heat. Tectonophysics 251, 153–159.
Parker, R.L., 1992. Geophysical Inverse Theory. Princeton University Press.
Paul, J.D., Roberts, G.G., White, N., 2014. The African landscape through space and time. Tectonics 32. https://doi.org/10.1002/2013TC003479.
Pekeris, C.L., 1935. Thermal convection in the interior of the Earth. Geophys. Suppl. Mon. Not. R. Astron. Soc. 3, 343–367.
Plank, T., Forsyth, D.W., 2016. Thermal structure and melting conditions in the mantle beneath the basin and range province from seismology and petrology. Geochem. Geophys. Geosyst. 17. https://doi.org/10.1002/2015GC006205.
Priestley, K., McKenzie, D., 2006. The thermal structure of the lithosphere from shear wave velocities. Earth Planet. Sci. Lett. 244, 285–301.
Pritchard, D.P., Roberts, G.G., White, N., Richardson, C.N., 2009. Uplift histories from river profiles. Geophys. Res. Lett. 36. https://doi.org/10.1029/2009GL040928.
Replumaz, A., Karason, H., van der Hilst, R.D., Besse, J., Tapponnier, P., 2004. 4-D evolution of SE Asia's mantle from geological reconstructions and seismic tomography. Earth Planet. Sci. Lett. 221, 103–115.
Richards, M.A., Hager, B.H., 1984. Geoid anomalies in a dynamic Earth. J. Geophys. Res. 89, 5987–6002.
Ritsema, J., van Heijst, H.J., Woodhouse, J.H., 1999. Complex shear wave velocity structure imaged beneath Africa and Iceland. Science 286 (5446), 1925–1928.
Roberts, G.G., White, N.J., 2010. Estimating uplift rate histories from river profiles using African examples. J. Geophys. Res. 115 (B02406). https://doi.org/10.1029/2009JB006692.
Roberts, G.G., Paul, J.D., White, N., Winterbourne, J., 2012. Temporal and spatial evolution of dynamic support from river profiles: a framework for Madagascar. Geochem. Geophys. Geosyst. 13 (1). https://doi.org/10.1029/2012GC004040.
Roberts, G.G., White, N.J., 2017. The importance of long wavelength processes in generating landscapes. Geophys. Res. Abstr. 19, EGU2017-4787.
Rudge, J.F., Shaw Champion, M.E., White, N., McKenzie, D., Lovell, B., 2008. A plume model of transient diachronous uplift at the Earth's surface. Earth Planet. Sci. Lett. 267, 146–160.
Rudge, J.F., Roberts, G.G., White, N.J., Richardson, C.N., 2015. Uplift histories of Africa and Australia from linear inverse modeling of drainage inventories. J. Geophys. Res., Earth Surf. 120. https://doi.org/10.1002/2014JF003297.
Schaeffer, A.J., Lebedev, S., 2013. Global shear speed structure of the upper mantle and transition zone. Geophys. J. Int. 194, 417–449.
Simons, W.J.F., Socquet, A., Vigny, C., Ambrosius, B.A.C., Haji Abu, S., Promthong, C., Subarya, C., Sarsito, D.A., Matheussen, S., Morgan, P., Spakman, W., 2007. A decade of GPS in Southeast Asia: resolving Sundaland motion and boundaries. J. Geophys. Res. 112 (B06420). https://doi.org/10.1029/2005JB003868.
Soeria-Atmadja, R., Noeradi, D., Priadi, B., 1999. Cenozoic magmatism in Kalimantan and its related geodynamic evolution. J. Asian Earth Sci. 17, 25–45.
Spasojevic, S., Gurnis, M., 2012. Sea level and vertical motion of continents from dynamic earth models since the Late Cretaceous. AAPG Bull. 96 (11), 2037–2064.
Steinberger, B., 2007. Effect of latent heat release at phase boundaries on flow in the Earth's mantle, phase boundary topography and dynamic topography at the Earth's surface. Phys. Earth Planet. Inter. 164, 2–20.
Steinberger, B., Conrad, C.P., Tutu, A.O., Hoggard, M.J., 2017. On the amplitude of dynamic topography at spherical harmonic degree two. Tectonophysics. https://doi.org/10.1016/j.tecto.2017.11.032.
Tang, Q., Zheng, C., 2013. Crust and upper mantle structure and its tectonic implications in the South China Sea and adjacent regions. J. Asian Earth Sci. 62, 510–525.
Tapley, B., Ries, J., Bettadpur, S., Chambers, D., Cheng, F., Condi, B., Gunter, Z., Kang, P., Nagel, R., Pastor, T., Pekker, S., Poole, S., Wang, F., 2005. GGM02 – an improved Earth gravity field model from GRACE. J. Geod. 79 (8), 467–478.
Yang, T., Gurnis, M., Zahirovic, S., 2016. Mantle-induced subsidence and compression in SE Asia since the early Miocene. Geophys. Res. Lett. 43, 1901–1909. https://doi.org/10.1002/2016GL068050.
Yang, T., Gurnis, M., 2016. Dynamic topography, gravity and the role of lateral viscosity variations from inversion of global mantle flow. Geophys. J. Int. 207 (2), 1186–1202. https://doi.org/10.1093/gji/ggw335.
Wheeler, P., White, N., 2000. Quest for dynamic topography: observations from Southeast Asia. Geology 28 (11), 963–966.
Wheeler, P., White, N., 2002. Measuring dynamic topography: an analysis of Southeast Asia. Tectonics 21 (5). https://doi.org/10.1029/2001TC900023.
Whipple, K.X., Tucker, G.E., 1999. Dynamics of the stream-power river incision model: implications for height limits of mountain ranges, landscape response timescales, and research needs. J. Geophys. Res. 104 (B8), 17,661–17,674.
Willett, S.D., McCoy, S.W., Perron, J.T., Goren, L., Chen, C.-Y., 2014. Dynamic reorganization of river basins. Science 343. https://doi.org/10.1126/science.1248765.
Wilson, M.E.J., Chambers, J.L.C., Evans, M.J., Moss, S.J., Nas, D.S., 1999. Cenozoic carbonates in Borneo: case studies from northeast Kalimantan. J. Asian Earth Sci. 17, 183–201.
Wilson, M.E.J., Moss, S.J., 1999. Cenozoic palaeogeographic evolution of Sulawesi and Borneo. Palaeogeogr. Palaeoclimatol. Palaeoecol. 145, 303–337.